Cardiac fibroblasts cellular anisotropy is determined by YAP-dependent cellular contractility and ECM production

Daniel Pereira-Sousa[a,b], Pau Guillamat[c], Francesco Niro[a,b,d], Vladimír Vinarský[a], Soraia Fernandes[a,e], Marco Cassani[a,e], Stefania Pagliari[a,d], Xavier Trepat[c,f,g],Marco Rasponi[h], Jorge Oliver-De La Cruz[a,c, *], Giancarlo Forte[a,d, *]

[a]Center for Translational Medicine (CTM), International Clinical Research Centre (ICRC), St. Anne´s Hospital, Brno, Czech Republic.
[b]Faculty of Medicine, Department of Biomedical Sciences, Masaryk University, 62500, Brno, Czech Republic.
[c]Institute for Bioengineering of Catalonia, The Barcelona Institute for Science and Technology, Barcelona 08028, Spain.
[d]School of Cardiovascular and Metabolic Medicine & Sciences, King's College London, London SE5 9NU, UK.
[e]Department of Chemical Engineering, The University of Melbourne, Victoria, 3010, Australia.
[f]Institució Catalana de Recerca i Estudis Avançats (ICREA), Barcelona, Spain
[g]Centro de Investigación Biomédica en Red en Bioingeniería, Biomateriales y Nanomedicina (CIBER-BBN), 08028 Barcelona, Spain
[h]Department of Electronics, Information and Bioengineering, Politecnico di Milano, Via Ponzio 34/5, Milan 20133, Italy
*joliver@ibecbarcelona.eu
*giancarlo.forte@kcl.ac.uk

ABSTRACT

Cardiac fibroblasts (CFbs) determine the topological arrangement and the anisotropy of the heart tissue, features which are essential for maintaining tissue integrity and function, primarily through the production and remodeling of the extracellular matrix (ECM). Under pathological conditions, CFbs can activate into myofibroblasts, which promote maladaptive ECM remodeling, a process which may lead to heart failure. Although the mechanosensitive Yes-Associated Protein (YAP) has been implicated in CFb activation, its role in the organization of CFbs and in their ability to deposit cardiac ECM remains unexplored. We investigated the effects of YAP genetic deletion on cardiac fibroblast phenotype and function by generating CFbs from wild-type (WT) and YAP knockout (KO) human embryonic stem cells (hESCs). We found that YAP depletion impaired CFbs differentiation by reducing the expression of cardiogenic markers. Additionally, we demonstrated that YAP expression is required for monolayer alignment of CFbs. Transcriptomic analysis further revealed that YAP is essential for the regulation of ECM- and contractility-related genes, and that its absence resulted in reduced ECM deposition, diminished anisotropy, and decreased force generation. Pharmacological inhibition of contractility closely mirrored YAP KO phenotype, suggesting that YAP regulates both monolayer organization and ECM structure through its control over contractility. These findings underscore the critical role of the mechanosensor YAP in maintaining the supracellular organization of CFbs and the mechanical integrity of cardiac tissue.

Keywords: Cardiac fibroblasts, extracellular matrix, YAP, nematic order, matrix anisotropy, cell contractility.

Introduction

Cardiac fibroblasts (CFbs) are the most numerous cell type in the heart [1] and play a critical role in maintaining its structural and functional integrity. They contribute to heart tissue organization during development by migrating into the myocardium, where, through complex multicellular interactions with the other cardiac cells, contribute to the correct 3D arrangement of cardiomyocytes within the ventricular walls [2, 3]. Eventually, they align parallel to the direction of myocardial fibers, establishing themselves as resident cardiac fibroblasts [4, 5]. The topological arrangement of fibroblasts and myocytes is conserved throughout postnatal life, and it is essential for heart functionality by maintaining the homeostasis of the extracellular matrix (ECM). Indeed, CFbs produce collagen fibers that align with their elongated morphology, providing crucial structural, electrical, and mechanical support to the cardiomyocytes [6]. This orientation contributes to the anisotropic mechanical properties of the ECM, essential for efficient force transmission and load bearing in the cardiac tissue [7].

Upon heart injury, CFbs undergo rapid proliferation and differentiate into contractile myofibroblasts, which are the main drivers of cardiac fibrosis [8, 9]. Myofibroblasts produce and deposit excessive ECM components, including collagens and matrix metalloproteinases (MMPs) [10]. This process results in the generation of a stiff, non-compliant and disorganized ECM with reduced anisotropy [11]. The disrupted structural organization and mechanical properties further exacerbate cardiac dysfunction [12-17] by impairing cardiomyocyte contractility and electrical conduction [10].

The mechanosensitive transcriptional co-activator Yes-associated protein (YAP) has emerged as a critical regulator of CFb activation and fibrosis [18, 19]. As the key effector of the Hippo signaling pathway, YAP responds to mechanical cues from the ECM, translocating to the nucleus where it modulates gene expression in conjunction with other transcription factors like TEADs [20-25]. YAP has been shown to be crucial for cardiac development [18, 19] and its sustained activity is known to promote CFb proliferation and differentiation into myofibroblasts [20-25]. Additionally, YAP was reported to induce the expression of myofibroblast gene programs in response to topographic cues, suggesting its role in influencing CFb functionality *via* mechanotransduction [26]. Our group recently demonstrated that YAP shuttling to the nucleus of CFbs in the failing human heart contributes to exacerbate ECM remodeling [27].

Nevertheless, the role of YAP in guiding the topological arrangement of CFbs in the heart or the anisotropy and directionality of the ECM remains unexplored.

This study investigates how YAP regulates both the spatial organization of CFbs within monolayers and the ECM architecture, focusing on their anisotropy and long-range orientational (nematic) order, known to be key organizers of fibroblast collectives [28]. We explore how YAP modulates the interplay between ECM deposition by CFbs and cellular contractility and examine their contribution to the collective cell organization. Finally, we study YAP involvement in the ECM disarrangement produced by the activation of fibroblasts mediated by transforming growth factor (TGF)-β signaling. By elucidating the specific mechanisms through which YAP influences CFbs alignment and ECM organization, this study sheds light on the complex interplay between ECM remodelling and CFbs in the diseased heart.

Results

YAP depletion impairs the acquisition of the cardiac fibroblast phenotype.

To study the role of YAP in CFb function, we took advantage of wild-type (WT) and clustered regularly interspaced short palindromic repeat (CRISPR) YAP knockout (YAP KO) human embryonic stem cells (hESCs) and differentiated them into CFbs using an established protocol [29] (Fig. 1A). This protocol involves the inhibition of glycogen synthase kinase 3 (GSK3α) inhibition using CHIR99021 to induce cardiac mesoderm specification, followed by the treatment with basic fibroblast growth factor (bFGF) to obtain CFbs via second heart field progenitors [29]. Both WT and YAP KO CFbs appeared as adherent cells with an elongated, spindle-shaped aspect characteristic of fibroblasts (Fig. 1B).

Flow cytometry analysis was conducted to phenotypically characterize the cell lines generated based on the expression of hematopoietic (CD45), endothelial (CD31), and various mesenchymal markers (CD90, CD73, CD105, CD146) (Fig. 1C). As expected, the expression of CD45 and CD31 was negligible. Low levels of CD73 and CD146 were also found, while a significantly higher percentage of CD105 expressing cells was detected in WT CFbs in comparison to YAP KO population (8.1 ± 1.5% vs. 1.1 ± 0.3%). In contrast, both cell populations showed high levels of CD90 expression (99.1 ± 0.2% vs. 99.8 ± 0.1%).

In addition, both cell populations were positive for platelet derived growth factor receptor α (PDGFR α) and discoidin domain receptor tyrosine kinase 2 (DDR2) (Fig. 1D, E). However, the expression of GATA4, a cardiogenic transcription factor essential for heart development and usually expressed in CFbs [30, 31], was undetectable in YAP KO CFbs contrasting the results obtained for WT CFbs (34.0 ± 0.8% $GATA4^{+}$) (Fig. 1E).

These findings suggest that while YAP is dispensable for the differentiation of hESC-derived cells into cardiac fibroblasts, it plays a fundamental role in defining their molecular identity.

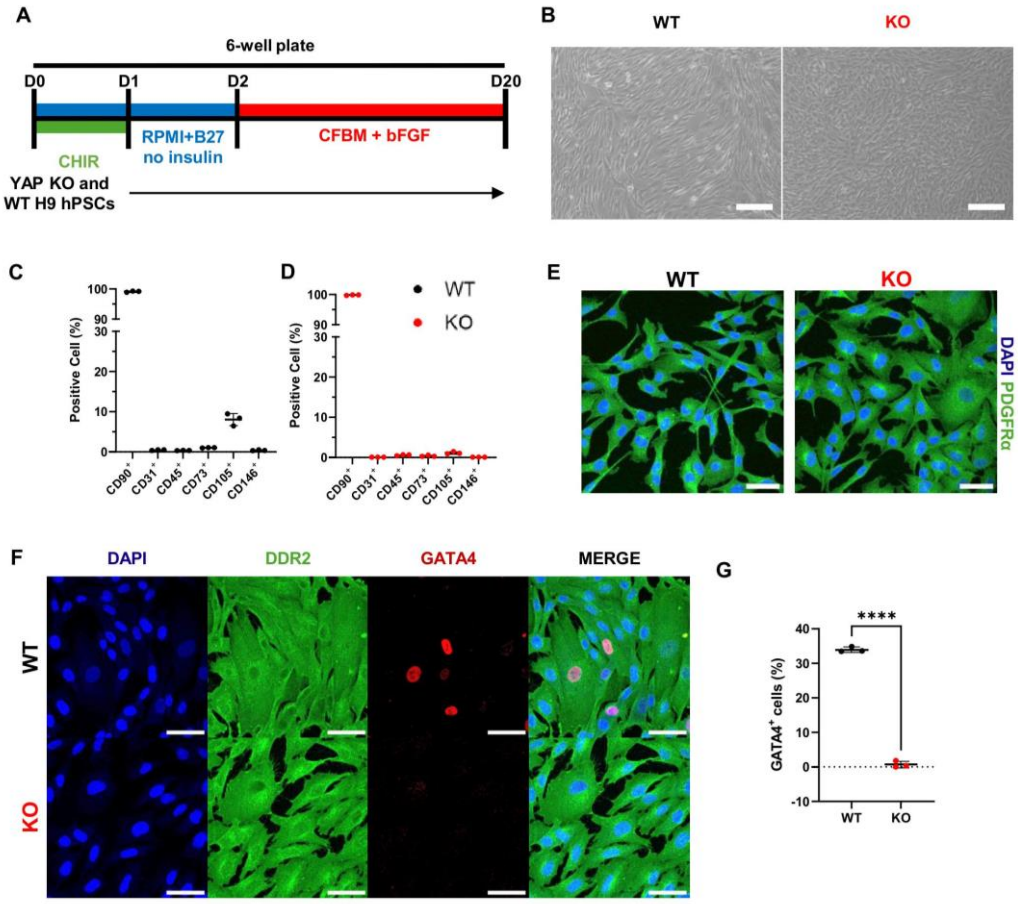

Figure 1: YAP depletion disrupts the acquisition of cardiogenic markers in cardiac fibroblasts. **(A)** Differentiation protocol of cardiac fibroblasts. **(B)** Representative brightfield images of WT and YAP KO CFbs. Scale bars: 100µm. **(C)** Dotplot of the quantification of cell percentage expressing CD90, CD45, CD31, CD73, CD105 and CD146 in YAP WT CFbs obtained from each differentiation (YAP WT CFbs N=3). **(D)** Dotplot of the quantification of cell percentage expressing CD90, CD45, CD31, CD73, CD105 and CD146 in YAP KO CFbs obtained from each differentiation (YAP KO CFbs N=3). **(E)** Representative confocal images of DAPI (blue) and PDGFRα (green) in YAP WT and KO CFbs. Scale bars: 50µm. **(F)** Representative confocal images of DAPI (blue), DDR2 (green) and GATA4 (red) in YAP WT and KO CFbs. Scale bars: 50µm. **(G)** Quantification of GATA4 expressing cells in YAP WT and KO CFbs (WT/KO CFbs N=3). Statistical analysis performed by unpaired t test.

YAP depletion disrupts the nematic order in monolayers of CFbs

The study of the organization of cells in monolayers provides invaluable insights into the fundamental principles that govern cell alignment and collective behavior, reflecting key aspects of multicellular organization [32]. Fibroblasts in high-density cultures align with each other, leading to highly anisotropic monolayers exhibiting long-range orientational (nematic) order [33]. To explore the role of YAP in regulating the spatial organization of CFbs, we assessed the effects of its genetic depletion on the single cell morphology and collective organization and order in monolayers.

We started our examination by evaluating the shape of single cells by seeding YAP KO and WT CFbs at low density (5000 cells/cm^2) on gelatin-coated tissue culture polystyrene dishes. The morphological analysis of isolated cells revealed that, although YAP KO cells displayed a significantly reduced spreading area (3711 ± 1619 µm^2 in WT CFbs vs. 2861 ± 879 µm^2 in YAP KO CFbs), there were no differences in shape between WT and YAP KO CFbs (Fig.1E and Fig. 2A).

However, in monolayers, WT CFbs exhibited an elongated morphology and directional alignment, leading to nematic order (Fig. 2B, left panels)[33]. Interestingly, this organization was disrupted upon YAP depletion (Fig. 2B, right panels), showing a significantly lower anisotropy than in WT monolayers (Fig. 2C). This led to larger number of disorganized regions, with nematic order Q <0.5 (Fig. 2D). Additionally, the spatial autocorrelation function of orientation revealed a faster decay in YAP KO cell monolayers, indicating a reduction in the characteristic size of nematically-aligned multicellular domains, with sizes roughly three-fold smaller than in the WT case (Fig. 2E). These results suggest that YAP expression is crucial for maintaining cell anisotropy and long-ranged nematic order in CFb monolayers.

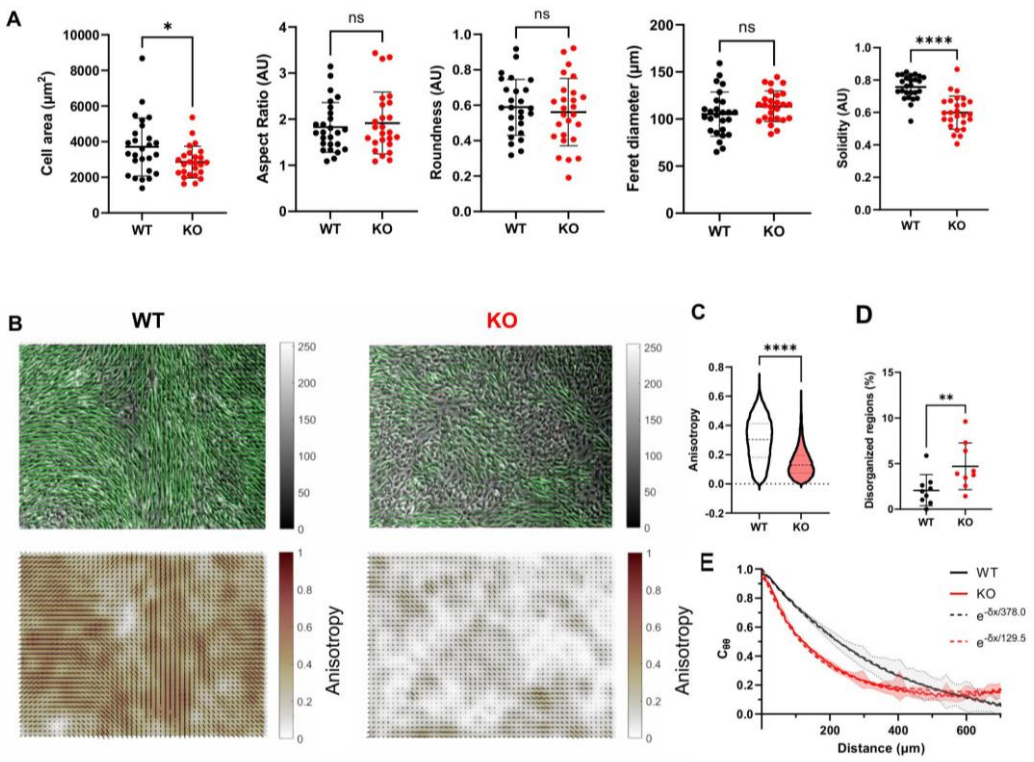

Figure 2:Depletion of YAP disrupts cell monolayer nematic ordering in cardiac fibroblasts. (A) Dotplots of cell area, aspect ratio, roundness, Feret diameter and solidity of YAP WT and KO CFbs. Statistical analysis performed by unpaired t test. **(B)** Representative brightfield images with vector field of orientations and respective maps of Anisotropy values in YAP WT and KO CFbs. **(C)** Violin plots of the quantification of anisotropy of the cell monolayer of YAP WT and KO CFbs (YAP WT/KO CFbs N=3). Statistical analysis performed by unpaired t test. **(D)** Dotplot of quantification of the percentage of disorganized regions (Q<0.5) in YAP WT and KO CFbs (N=3 for both YAP WT and KO CFbs). Statistical analysis performed by unpaired t test. **(E)** Spatial autocorrelation functions of orientation for YAP WT and KO CFbs.

YAP regulates extracellular matrix gene expression and organization.

YAP was observed to shuttle to the nucleus of heart cells in the diseased heart following ECM remodeling [27]. Here, YAP is known to act as a transcription co-factor [34]. We analyzed YAP transcriptional activity in CFbs to further investigate the molecular mechanisms leading to the disruption of cellular alignment caused by YAP depletion. We performed bulk RNA sequencing of WT and YAP KO CFbs and compared their transcriptional landscape to adult human cardiac fibroblasts (HCFs) using principal component analysis (PCA, Supplementary Fig. 1A). Both differentiated WT and YAP KO CFbs differed markedly from HCFs, suggesting that YAP WT and KO CFbs retain a rather immature phenotype compared to their adult counterpart. This was further

investigated by analyzing the expression of subsets of CFbs-specific markers. Both WT and YAP KO CFbs expressed core fibroblast markers such as *THY1* (CD90), *PDGFRA*, *DDR2* and *VIM*. However, YAP KO CFbs exhibited reduced expression of genes associated with their activation, i.e. *FAP* and *ACTA2* (Fig. 3A). Moreover, we detected significant differences in the expression of markers associated with cardiac fibroblast identity. In particular, YAP depletion determined reduced expression of transcriptional factors *WT1*, *GATA4*, *NKX2.5* and *TBX5* (Supplementary Fig. 1C), suggesting that YAP is necessary for the expression of characteristic cardiogenic genes [31]. The differential expression analysis between WT and YAP KO CFbs lead to the identification of 950 differentially expressed genes (DEGs, 450 downregulated and 500 upregulated in WT cells, Supplementary Table 1) of which only 21.6% were previously identified as direct YAP targets (Supplementary Fig. 1B). Functional annotation of the DEGs highlighted YAP as a key regulator of the cell-matrix interface, with significant changes in the expression of genes associated with ECM (collagen-related extracellular matrix and basement membrane) and cell migration (cell leading edge, Fig. 3B, Supplementary Table 2). Network functional enrichment analysis revealed a dense interconnection among genes in these categories (Supplementary Fig. 1C).

Furthermore, approximately 11% of all genes found dysregulated in YAP KO CFbs were identified as matrisome proteins that were then annotated to several matrisome categories [35], namely collagens, ECM regulators, secreted factors, ECM-affiliated proteins, ECM glycoproteins and proteoglycans (Fig. 3C, Supplementary Table 3). In detail, collagens (*COL1A1*, *COL1A2*, *COL4A1*), proteoglycans (*DCN*, *BGN*) and glycoproteins (*LAMA1*, *LAMA4*, *LAMC2),* that are normally associated with increased fibrotic ECM deposition [36], were found upregulated. Interestingly, several matrix metalloproteinases (*MMP1, MMP11 and MMP19*) and a disintegrin and metalloproteinase with thrombospondin motifs (ADAMTS) proteins (*ADAMTS1, ADAMTS9, ADAM8*) were found significantly downregulated, indicating that the deletion of YAP might disrupt ECM production by CFbs [37].

To test whether YAP depletion impacted ECM deposition, we adopted a decellularization protocol our group described in a previous study [38]. Decellularized extracellular matrices (dECMs) were stained for the most represented structural components of cardiac ECM, namely, fibronectin (FN), collagen I, and collagen IV (Fig. 3F, Supplementary Fig. 1D). Image analysis of the area covered by each ECM protein revealed that YAP depletion in CFbs led to a significant reduction in FN (31.9 ± 2.1% in WT CFbs vs. 25.4 ± 4.3% in YAP KO CFbs) and COL IV (31.7 ± 1.8% in WT CFbs vs. 25.9 ± 3.4% in YAP KO CFbs) deposition. Furthermore, the quantification of the average intensity of protein-covered areas also showed a significant reduction in collagen I deposition (9.5 ± 2.0% in WT CFbs vs. 6.4 ± 0.9% in YAP KO CFbs) (Fig. 3G-H). YAP depletion led to a significant loss of ECM alignment, with YAP KO CFbs producing a more isotropic matrix compared to WT CFbs (0.30 ± 0.10 in WT CFbs vs. 0.11 ± 0.06 in YAP KO CFbs). Additionally, the absence of YAP increased fiber curvature and number of branch endpoints per ECM fiber length (Supplementary Fig. 1F) [39]. Altogether, these results indicate that YAP expression in cardiac fibroblasts contributes to ECM deposition and organization.

Since YAP KO CFbs demonstrated to have disrupted nematic ordering and ECM organization, we next set to investigate whether both these processes were spatially correlated. We hence sought to quantify the angular differences between the orientation of actomyosin stress fibers, ECM fibers and nuclei in confluent monolayers of WT and YAP KO CFbs (Fig. 3H). YAP KO CFbs showed a broader distribution of the angular difference between the orientation of the nuclei and actin filaments, indicating a loss of coordinated cytoskeletal and nuclear orientation required for cell

polarity and organized behavior within the monolayer (Fig. 3I). When comparing the distribution of angular differences between the F-actin cytoskeleton and the deposited fibronectin (FN), both WT and YAP KO CFbs exhibited a sharp peak centered around 0°, indicating that cells and matrix are generally well-aligned in both monolayers (Fig. 3J). However, the peak in YAP KO CFbs appeared slightly broader than in WT cells, suggesting reduced alignment between actin and ECM, contributing to a more isotropic matrix structure in YAP-depleted cells. Overall, these results indicate that the cytoskeletal disorganization in YAP KO CFbs is mirrored in the ECM alignment, leading to the deposition of a less anisotropic matrix.

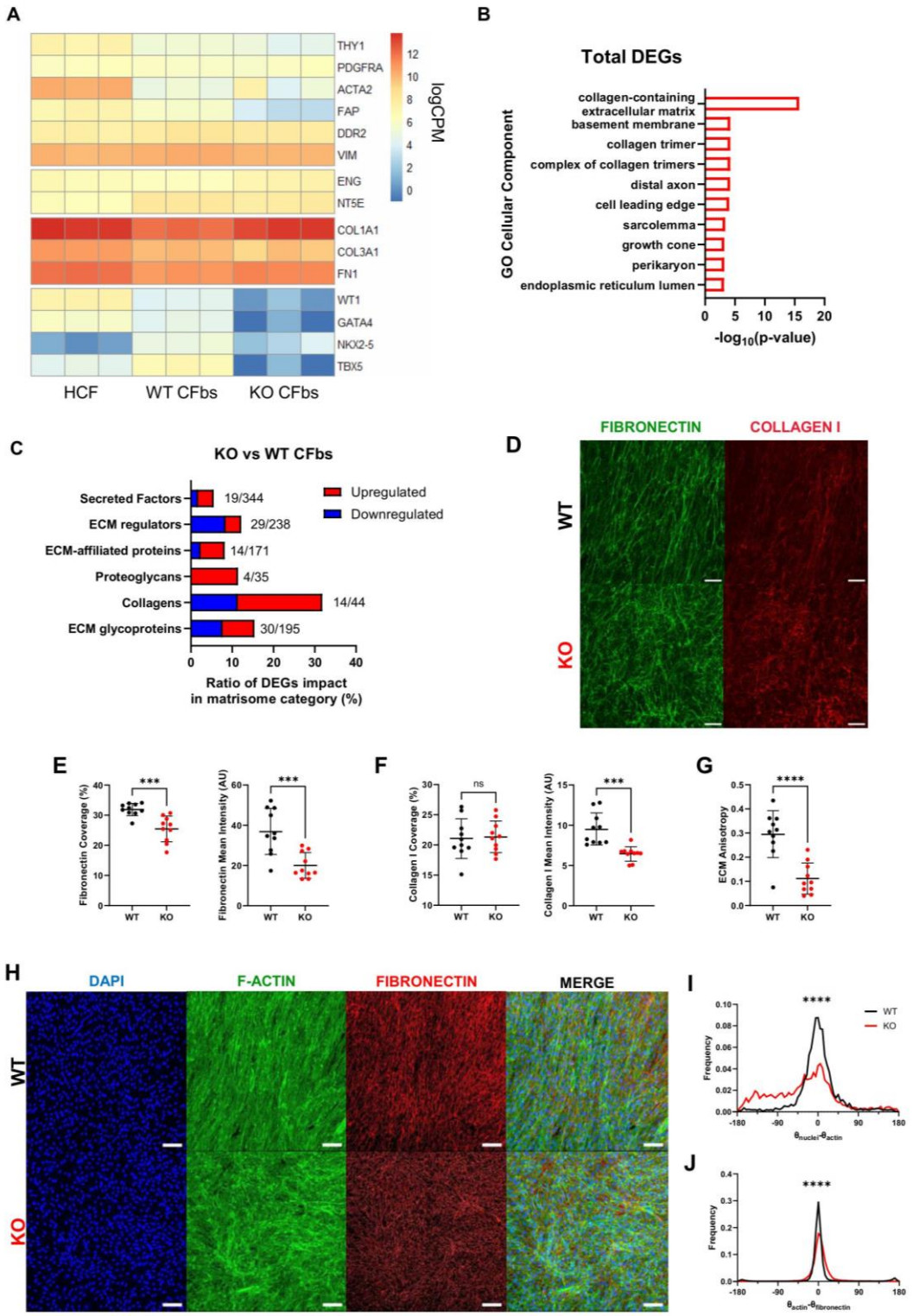

Figure 3: YAP influences extracellular gene expression and organization. (A) Heatmap of gene expression of selected fibroblast and cardiac markers obtained WT and YAP KO CFbs together with adult primary cell line of human cardiac fibroblasts (HCF) (YAP WT/KO CFbs N=3; HCF N=3). **(B)** Barplot of most enriched Gene Ontology term in Cellular Components compartment using differently expressed genes obtained from comparing YAP KO vs WT CFbs. **(C)** Bar plot showing the ratio of matrisome DEGs that are upregulated (red) and downregulated (blue) after YAP depletion in CFbs in each matrisome category. The numbers beside the bar show total detected genes/total genes in the respective matrisome category. **(D)** Representative confocal images of decellularized extracellular matrix produced by YAP WT and KO CFbs in control conditions stained for fibronectin (green) and collagen I (red). Scale bars: 100µm. **(E)** Dotplots of the coverage and mean intensity of fibronectin in YAP WT and KO CFbs in control conditions. (YAP WT/KO CFbs N=3). Statistical analysis performed by unpaired t-test. **(F)** Dotplots of the coverage and mean intensity

of collagen I in YAP WT and KO CFbs in control conditions (YAP WT/KO CFbs N=3). Statistical analysis performed by unpaired t-test. **(G)** Dotplots of ECM anisotropy in YAP WT and KO CFbs in control conditions (YAP WT/KO CFbs N=3). Statistical analysis performed by unpaired t-test. **(H)** Representative confocal images of YAP WT and KO CFbs stained for DAPI (blue), F-actin (green) and fibronectin (red). Scale bars: 100µm. **(I)** Graph showing angle distribution of the difference between nuclei and F-actin orientation in YAP WT and KO CFbs. Statistical analysis performed by Watson-Wheeler test. **(J)** Graph showing angle distribution of the difference between F-actin and fibronectin orientation in YAP WT and KO CFbs. Statistical analysis performed by Watson-Wheeler test.

YAP deletion impairs cardiac fibroblast contractility by impacting focal adhesions and myosin phosphorylation

Since cytoskeletal dynamics is known to be responsible to influence other cell functions such as cell contractility and cell adhesion via focal adhesions (FAs) [40, 41], we sought to investigate the impact of YAP in genes related to these processes. YAP depletion led to the downregulation of key contractility-related genes *MYLK*, *LIMK1*, *ABLIM3*, and *SHROOM2* in our RNA-sequencing data. All these genes are regulators of actin-myosin dynamics and cytoskeletal organization. This was accompanied by the upregulation of compensatory genes such as RHOB (Fig. 4A).

Our group previously demonstrated that YAP targets the transcription of genes involved in FAs and cytoskeletal assembly in different cell types [42, 43]. Despite not observing changes in the protein expression of FA-related proteins (Supplementary Fig 2A and B), we decided to study the cellular adhesion properties of YAP-depleted cells further by staining the cells for vinculin, a protein involved in the formation of FAs. The analysis of the vinculin-stained cells showed a significant reduction in FA area in YAP KO CFbs (0.09 ± 0.02 in WT CFbs vs 0.06 ± 0.01 in YAP KO CFbs) and density (0.10 ± 0.02 μm^{-2} in WT CFbs vs. 0.07 ± 0.01 μm^{-2} in YAP KO CFbs) (Fig. 4B-C). These findings suggest that cellular adhesion was compromised after YAP depletion.

Moreover, the protein expression of phosphorylated (active) non-muscle myosin II (pMLC2), one of the main drivers of cell contractility, was substantially reduced in YAP KO cells (1.0 ± 0.1 in WT CFbs vs. 0.8 ± 0.2 in YAP KO CFbs) (Fig. 4D). In WT CFbs, pMLC2 was evenly distributed along the stress fibers. However, in YAP KO cells, pMLC2 largely accumulated at the cell edges (Figure 3E), with a threefold higher protein distribution at the cell border. This disclosed a peripherally localized cellular contractility pattern, indicating an alteration in the myosin-driven contraction network within the cell (Fig. 4E). To elucidate whether the above-mentioned findings created a measurable impact on cell contractility, a collagen contraction assay was performed. To this end, WT and YAP KO CFbs were embedded in a collagen gel, the contraction of which was measured after 24 hours. The results demonstrated a significant decrease in the contractile capabilities of YAP KO CFbs (40.3 ± 1.9%) as compared to the WT CFbs (50.3 ± 2.4 %, Fig. 4F).

Altogether, these data show that the reduced number of FAs and impaired phosphorylation of MLC2 affect the contractile capacity of YAP KO CFbs, as demonstrated by their diminished ability to remodel the surrounding ECM.

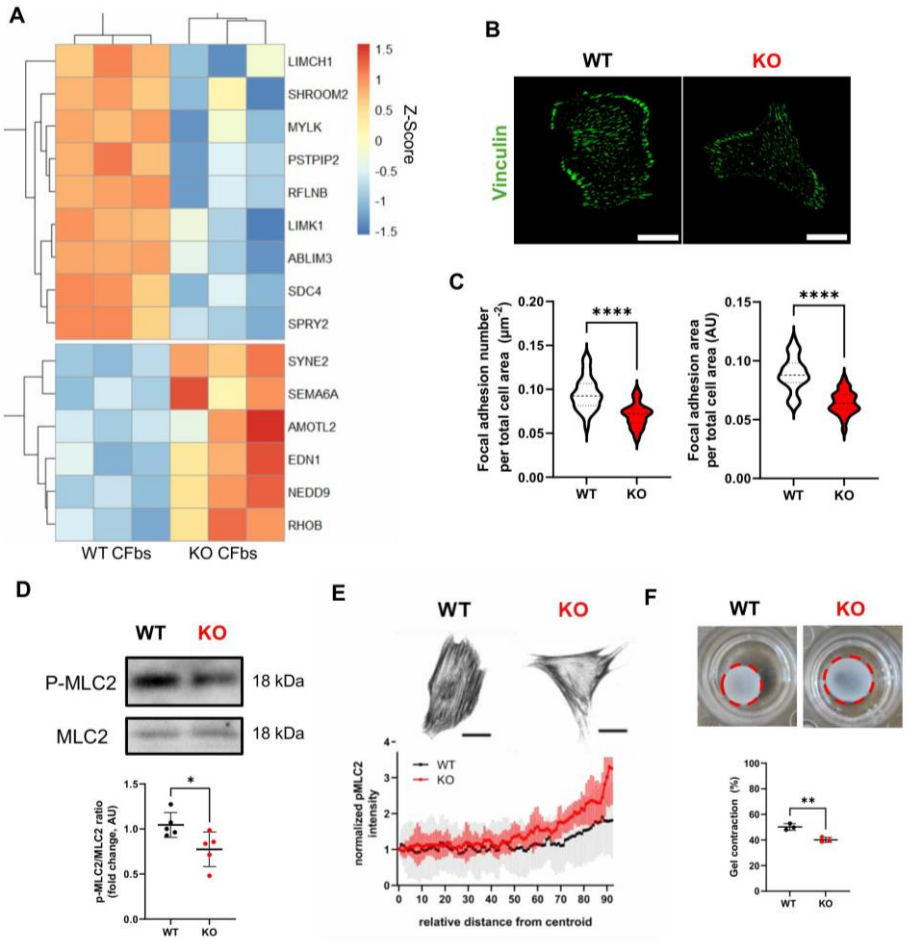

Figure 4. Deletion of YAP disrupts focal adhesion assembly and myosin functionality. (A) Heatmap of selected genes involved in cell contractility obtained by bulk RNASeq of WT and YAP KO CFbs. **(B)** Representative confocal images of YAP WT and KO CFbs stained for vinculin (green). Scale bars: 25 µm. **(C)** Violin plots of the quantification of focal adhesion number per total cell area and focal adhesion area per total cell area in YAP WT and KO CFbs. Statistical analysis performed by unpaired t-test. **(D)** Representative confocal images of YAP WT and KO CFbs stained for p-MLC2 and graph of normalized intensity as a function of relative distance to cell centroid in YAP WT and KO CFbs. Scale bars: 25 µm. **(E)** Representative blots of phospho-MLC2 and total MLC2 and the respective dotplot of the quantification of in YAP WT and KO CFbs (N=5). Statistical analysis performed by unpaired t-test. **(F)** Representative images of contracted collagen gels by YAP WT and KO CFbs at the 24h timepoint together with dotplots of the percentage of collagen gel contraction. Statistical analysis performed by unpaired t test.

The disruption of Contractility Is the Main Driver of Monolayer Disorganization in YAP-Depleted Cells

Cell contractility and ECM remodelling are interdependent processes required to maintain tissue architecture. While contractility influences ECM deposition and organization, the ECM provides mechanical feedback to regulate in turn cellular tension [17, 44]. Although these processes are interconnected, they are regulated by different pathways, making it essential to explore their individual impact on monolayer disorganization. To quantify these contributions, WT CFbs were treated with either β-Aminopropionitrile (BAPN), an inhibitor of the lysyl oxidase (LOX) ECM crosslinker family or blebbistatin (Bleb), an inhibitor of myosin ATPase activity (Fig. 5A). Here, YAP KO CFb monolayers were used as reference for monolayer disorganization. Both treatments resulted in a significantly reduced monolayer anisotropy, with myosin inhibition via Bleb more closely mimicking the effects of YAP genetic depletion (Fig. 5B). Consistently, the spatial autocorrelation function of orientation decayed faster with both treatments compared to the

control WT cells (Fig. 5C). The Bleb-treated monolayers led to a much faster decay, indicating a shorter propagation of nematic order, as observed for YAP KO cells (Fig. 5C).

Furthermore, the analysis of the dECM revealed that BAPN significantly reduced fibronectin coverage and increased the gaps (lacunarity) in WT CFbs as well as ECM complexity, confirming its effectiveness in inhibiting ECM deposition (Fig. 5D; Supplementary Figure 3). Interestingly, Bleb had a more pronounced impact on ECM anisotropy, indicating that - while BAPN effectively reduces ECM deposition - contractility plays a greater role in organizing the deposited ECM (Fig. 5E). These findings highlight that impaired contractility, rather than ECM deposition alone, dictates the disorganization of cell and ECM alignment following YAP depletion. This suggests a synergistic but hierarchical relationship in which contractility is the primary driver of organization at the cell and ECM level, while ECM deposition provides a scaffold that supports long-range multicellular order.

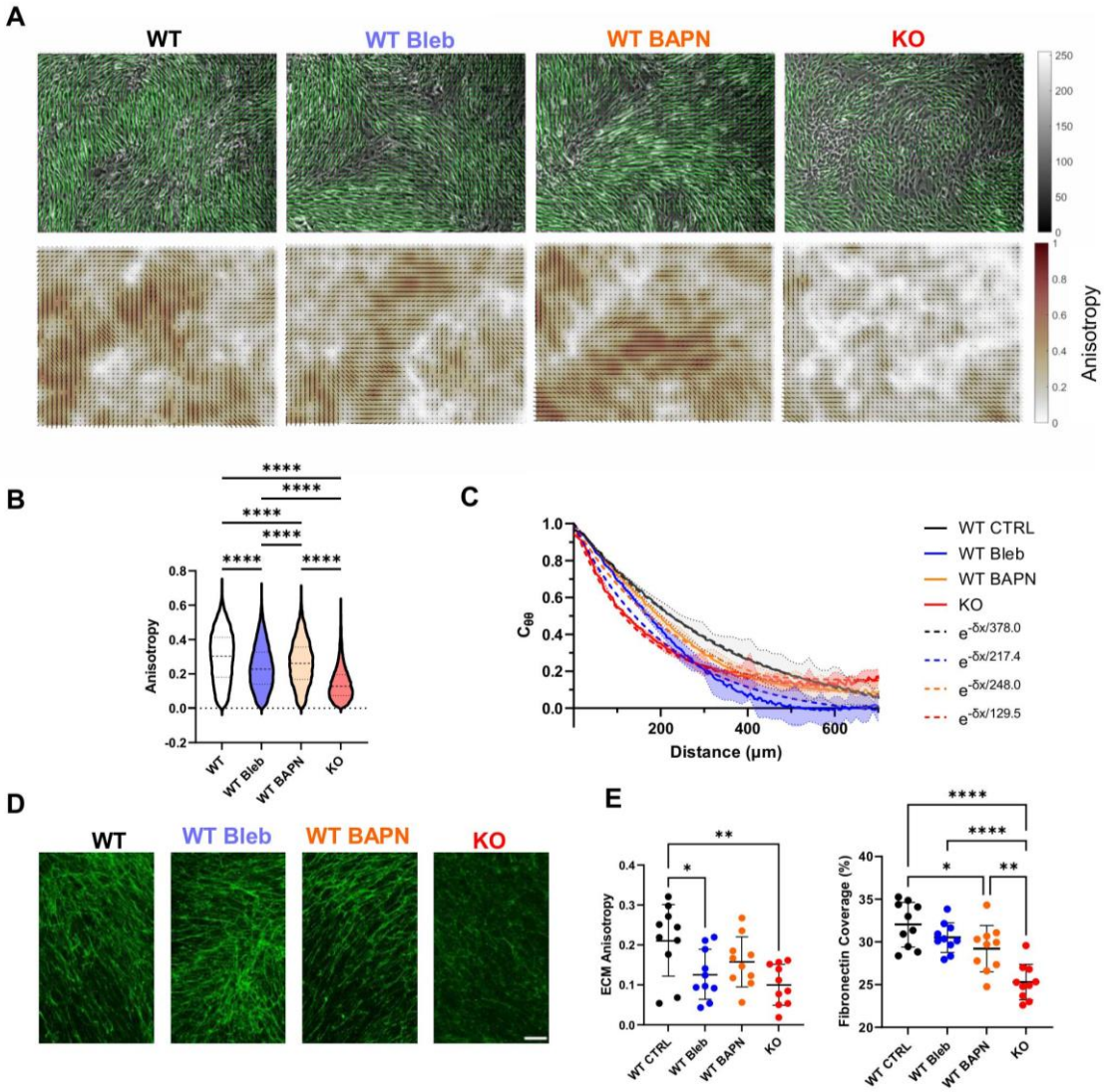

Figure 5. Inhibition of myosin phosphorylation by blebbistatin impacts cell monolayer and ECM organization. (A) Representative brightfield images with vector field of orientations and respective maps of anisotropy values in YAP WT CFbs, YAP WT CFbs treated with Blebbistatin, YAP WT CFbs treated with BAPN and KO CFbs. **(B)** Violin plots of the quantification of anisotropy of the cell monolayer of YAP WT CFbs, YAP WT CFbs treated with Blebbistatin, YAP WT CFbs treated with BAPN and KO CFbs (N=3 in all conditions). Statistical analysis performed by One-way ANOVA, followed by Tukey's multiple comparisons test. **(C)** Spatial autocorrelation functions of orientation for YAP WT CFbs, YAP WT CFbs treated with Blebbistatin, YAP WT CFbs treated with BAPN and KO CFbs. **(D)** Representative confocal

images of decellularized extracellular matrix produced by YAP WT CFbs, YAP WT CFbs treated with Blebbistatin, YAP WT CFbs treated with BAPN and KO CFbs in control conditions stained for fibronectin (green). Scale bars: 100µm. **(E)** Dotplots of the ECM anisotropy and coverage of fibronectin in YAP WT CFbs, YAP WT CFbs treated with Blebbistatin, YAP WT CFbs treated with BAPN and KO CFbs. (N=3 in all conditions). Statistical analysis performed by One-way ANOVA, followed by Tukey's multiple comparisons test.

YAP depletion modulates cardiac fibroblast activation and myofibroblast differentiation

Cardiac fibroblast activation to the myofibroblast phenotype is a hallmark of the fibrotic response in the heart, which is reported to be impacted by YAP [22], resulting in the production of stiff, non-compliant ECM with reduced anisotropy [8, 9]. To assess the role of YAP in cardiac fibroblast activation into myofibroblasts, and consequently in ECM remodeling, YAP KO and WT CFbs were exposed to activating and inhibitory conditions for 5 days. Activation (ACT) was induced by removing bFGF from the basal culture conditions (CTRL), which suppresses spontaneous fibroblast activation [45]. More stringent inhibitory (INH) conditions were established by combining bFGF with the TGF-β type I receptor inhibitor A83-01.

Confocal imaging revealed that the incorporation of α-SMA into the actin cytoskeleton, a key marker of myofibroblast differentiation, occurred only under activation conditions in both WT and YAP KO cells (Fig. 6A, B; Supplementary Figure 4A). This indicates that YAP is not required for stress fiber assembly. Flow cytometry analyses confirmed that α-SMA and FAP levels increased similarly in both WT and YAP KO cells under activation conditions (Fig. 6C, D), with no significant differences observed between control and inhibitory conditions, suggesting that bFGF can effectively inhibit fibroblast activation in this model.

The expression of *COL1A1*, *COL3A1*, and *CCN2*—key ECM components associated with fibroblast activation— and *ACTA2 (*α-SMA), was quantified by real-time polymerase chain reaction (RT-PCR). Both WT and YAP KO CFbs exhibited a significant upregulation of *ACTA2* and *COL3A1* under activation conditions, while no significant difference was observed in *COL1A1* expression. Notably, the expression of *CCN2*, a direct YAP-TEAD target, was found unchanged in YAP KO cells under activation (5.0 ± 0.9 in WT vs. 0.6 ± 0.1 in YAP KO), while increased significantly under the same experimental conditions in control cells. This result suggested that YAP modulates the regulation of specific target genes like CCN2 during activation.

When examining ECM deposition, FN matrix coverage remained unaltered for both WT and YAP KO CFbs (Fig. 6E, F), while an increase in the collagen I area was observed only in WT CFbs (Fig. 6E, G). However, the fluorescence intensity of fibers increased for both FN and collagen I in both cell populations (Fig. 6F, G). This increase in intensity, without a corresponding change in coverage, suggests enhanced fibrillogenesis, where each fiber contains more deposited material, resulting in visibly thicker fibers. Lastly, the difference in ECM alignment anisotropy between WT and YAP KO cells was lost under activation conditions (Fig. 6H), primarily due to greater variability in anisotropy among WT ECM samples, indicating a more inconsistent deposition pattern.

These findings suggest that while YAP depletion has effects on fibroblast activation, including reduced expression of key YAP target genes such as CCN2, compensatory signaling pathways might partially mitigate its impact, allowing for continued fibroblast activation and ECM remodeling.

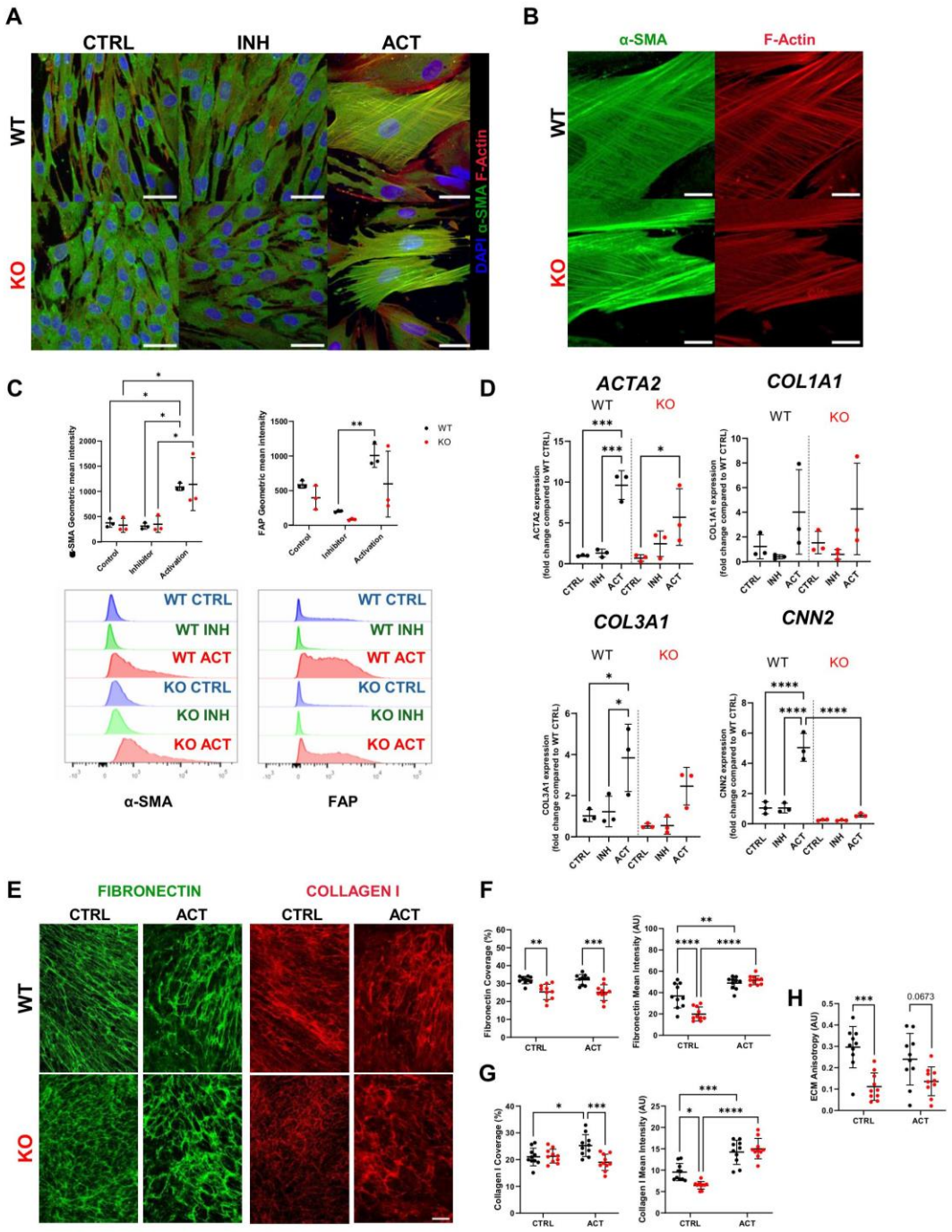

Figure 6. YAP depletion influences cardiac fibroblast activation. (A) Representative confocal images of YAP WT and KO CFbs in control, activation and inhibitory conditions stained for DAPI (blue), α-SMA (green) and F-actin (red). Scale bars: 50µm. **(B)** Representative inset of YAP WT and KO CFbs in activated condition to stained for α-SMA (green) and F-actin (red). Scale bars: 15µm. **(C)** Dotplot of the geometric mean intensity of α-SMA and FAP in YAP WT and KO CFbs in control, activation and inhibitory conditions together with histogram of α-SMA and FAP of these cell populations and an unstained control (YAP WT/KO CFbs N=3). Statistical analysis performed by 2-way ANOVA, followed by Tukey's multiple comparisons test. **(D)** Dotplots of the expression of ACTA2, COL1A1, COL3A1 and CCN2 in YAP WT and KO CFbs in control, activation and inhibitory conditions obtained by RT-PCR (N=3 in all condition). Statistical analysis performed by One-way ANOVA, followed by Tukey's multiple comparisons test. **(E)** Representative confocal images of decellularized extracellular matrix produced by YAP WT and KO CFbs in control and activation conditions stained for fibronectin (green) and collagen I (red). Scale bars: 100µm. **(F)** Dotplots of the coverage and mean intensity of the covered area of fibronectin in YAP WT and KO CFbs in control and activation conditions. (YAP WT/KO CFbs N=3). Statistical analysis performed by 2-way ANOVA, followed by Tukey's multiple comparisons test. **(G)** Dotplots of the coverage and mean intensity of the covered area of collagen I in YAP WT and KO CFbs in control and activation conditions. (YAP WT/KO CFbs N=3). Statistical analysis performed by 2-way ANOVA, followed by Tukey's multiple

comparisons test. **(H)** Dotplots of ECM anisotropy in YAP WT and KO CFbs and in control and activation conditions (YAP WT/KO CFbs N=3). Statistical analysis performed by 2-way ANOVA, followed by Tukey's multiple comparisons test.

Discussion

Cardiac fibroblasts (CFbs) are essential for maintaining the structural and functional integrity of the heart throughout development and into adulthood by ensuring the anisotropic properties of the ECM, which is critical for the heart efficiency and mechanical stability.

Our findings reveal that the mechanosensitive downstream effector of the Hippo pathway YAP is a central orchestrator of cellular alignment, ECM production and orientation in CFbs. Differentiating CFbs from both WT and YAP KO hESCs demonstrates that YAP depletion disrupts nematic order and reduces anisotropy within monolayers of CFbs, leading to the deposition of disorganized ECM. These observations underscore that ECM organization is contingent upon cytoskeletal alignment, with cytoskeletal disarray in YAP KO CFbs mirroring the diminished ECM anisotropy. This process is driven by YAP co-transcriptional activity, which regulates the expression of critical genes at the cell-matrix interface, including numerous matrisome components and contractile proteins.

Consequently, the absence of YAP causes decreased FA assembly of and impaired myosin-mediated contractility, in concordance with previous studies [42, 43, 46]. Similarly, the depletion of TFAP2C has been shown to disrupt the nematic order of cells and ECM organization, a process primarily guided by the TFAP2C-dependent regulation of fibroblast collisions [47]. Although TFAP2C was not differently expressed in YAP KO CFbs, both YAP and TFAP2C depletion reduce MLC2 phosphorylation, indicating the crucial role of cell contractility in maintaining nematic order and ECM organization. Moreover, our findings highlight the integral role of the ECM in monolayer organization, since the inhibition of ECM crosslinking, known to influence alignment [48], also disrupted monolayer organization. These results support models suggesting that simple collisions are insufficient for directing monolayer orientation [49]; instead, fibroblasts likely achieve collective alignment through nonlocal interactions facilitated by their modifications to the underlying ECM [49].

Therefore, our findings propose a hierarchical interaction in which CFb contractility drives both the monolayers and ECM organization, where ECM deposition provides the necessary guidance for sustaining specific supracellular nematic order. This model is supported by analogous behaviors observed in cancer-associated fibroblasts, where the deposition of fibronectin echoes their nematic organization and also provides a scaffold to maintain that specific nematic arrangement [50].

CFbs could differentiate from hESCs in the absence of YAP, although its expression remains critical for the acquisition of cardiogenic markers such as GATA4 and NKX2-5, which have been reported to significantly contribute to their fibrotic response and associated ECM remodeling activity [31, 51]. When exposed to TGF-β, YAP-depleted cells acquired myofibroblast phenotype, contrary to previous research [52]. However, YAP was still pivotal to induce the expression of CTGF/ CCN2, a direct target of YAP- TEAD complex [53, 54], and an essential driver of cardiac fibrosis [55]. These results align with prior studies demonstrating that TGF-β signaling is at least partially independent of YAP, despite the involvement of TEAD4 [56] and its paralog protein TAZ [57].

By elucidating the specific mechanisms through which YAP influences CFb alignment and ECM organization, this study opens pathways for developing targeted therapies that could manipulate cellular architecture to mitigate fibrosis and enhance cardiac function. Overall, this research serves as a foundational step in understanding the role of multicellular ordering in the

functionality of cardiac tissue. Future investigations will be necessary to refine our understanding of CFb behavior in cardiac tissues, potentially leading to the development of biomaterials to mimic the spatial dynamics of the cardiac environment.

Materials and Methods

Cell culture

The YAP knockout (YAP KO) and isogenic H9 (WT) human pluripotent stem cell lines were a kind gift of Miguel Ramalho-Santos and Han Qin. Their generation and culture were described previously [58]. The cells were maintained in an undifferentiated state by culturing them onto Matrigel Growth Factor Reduced (1:100 in DMEM/F12, Corning) in complete Essential 8™ Medium (E8, Thermo Fisher Scientific) containing penicillin/streptomycin (0.5%, VWR). hPSCs were frozen at a concentration of $1X10^6$ cells/cryovial in 90% KO-Serum + 10% DMSO inside Mr. Frosty™ Freezing Container (Thermo Fisher Scientific) at -80°C storage overnight. Cryovials were transferred 24 hours later for long-term storage in liquid nitrogen.
Human cardiac fibroblasts (HCF, ScienCell) were cultured in Claycomb media with L-glutamine supplemented with 10% FBS and 1% P/S.

Differentiation of WT and YAP KO cardiac fibroblasts

WT and YAP KO hPSCs were seeded on 6-well Matrigel-coated plates and maintained in culture until they reached 100% of confluency. Then, hPSCs were differentiated in CFbs following a previously published protocol [29]. Briefly, at day 0 of differentiation cell culture medium was switched from E8 to RPMI 1640 (Sigma-Aldrich) supplemented with penicillin/streptomycin, L-glutamine (2 mM, Biowest), B-27™ supplement minus insulin (1×, Thermo Fisher Scientific) and CHIR99021 (8µM, Sigma-Aldrich). Exactly 24h later media was replaced with RPMI B27 – INSULIN. On the evening of the second day of differentiation, the culture medium was switched from RPMI to FibroGro media + supplements (0% FBS) (Merck Millipore) + bFGF 75ng/mL (Peprotech). From day 3 to day 20 of differentiation, the growth medium was changed every second day until day 20. On day 20, flow cytometry was performed to validate the phenotype of CFbs differentiated from WT and YAP KO hPSCs (YAP KO/WT CFbs). YAP KO/WT CFbs were maintained in culture in T75 flasks with FibroGro medium + supplements (2% FBS) + bFGF 75ng/mL. Cells to be frozen were transferred to liquid nitrogen in 50% of media, 40% FBS and 10% DMSO.

Cardiac fibroblast activation assays and treatment

To assess the activation capabilities of YAP KO and WT CFbs, the cells were seeded at a density of 10^4 cells/cm^2 and maintained in culture for 5 days in FibroGro medium + 2% FBS either in the presence of 75ng/mL bFGF (control condition), or without bFGF (activation condition). Inhibitory condition was established by combining bFGF treatment with 500nM of TGF-β1 receptor inhibitor (A83-01, Tocris).
To observe cell monolayer organization, YAP KO and WT CFbs were seeded at a density of $5x10^3$ cells/cm^2 and cultured in control conditions and treated with Blebbistatin 10µM (Sigma-Aldrich) or β-Aminopropionitrile 1mM (BAPN, Sigma-Aldrich), and then grown at least 5 days until confluency. After that, brightfield images were obtained before fixing the cells in 4% paraformaldehyde (PFA) or decellularization.

Generation of decellularized ECM from fibroblasts

After culturing the fibroblasts in activation and control conditions, the cells were washed 3 times in ultrapure sterile water. Afterwards, decellularization solution composed of NH_4OH 20mM and Triton X 0,5% diluted in ultrapure sterile water was added to the plate for 10 minutes at room

temperature. The decellularized ECMs (dECMs) were then washed 3 times with PBS to remove the residues of the detergent and were fixed in PFA 4% for immunostaining.

Collagen gel contraction assay

The collagen contraction capabilities of the cells were evaluated using a previously described protocol [59]. Briefly, $2x10^5$ cells were resuspended in collagen I solution (rat tail, 1 mg/mL final concentration; Gibco) and 500 µL of this mixture was transferred to a 24-well plate for gelification with the addition of NaOH. The contraction of the gel was monitored overtime to assess ECM remodelling capabilities of the fibroblasts.

Flow Cytometry

For the staining of cell surface markers, cells were detached and counted. One to ten million cells were then collected into a 1.5 mL Eppendorf tube and washed in FACS buffer (0,5% FBS + EDTA 1:1000 in PBS). After centrifugation, the supernatant was removed, and the cell pellet was resuspended in 100µL of FACS buffer containing the conjugated primary antibody (Table 1). Cells were incubated in the dark for 30 minutes at 4 degrees, transferred into FACS tubes, and washed twice with FACS buffer. Samples were then acquired using BD FACSCanto II (Becton, Dickinson and Company, Franklin Lakes, NJ, USA), and cell populations were analysed with FlowJo v.10 (Tree Star). For the staining of intracellular markers, cells were washed in FACS buffer and then fixed in IC Fixation Buffer (BD Biosciences) for 20 minutes on ice in the dark. Cells were then washed in Permeabilization buffer 1X (BD Biosciences) and resuspended again in Permeabilization buffer 1X containing the conjugated antibody. After 30 minutes of incubation, cells were washed once in Permeabilization buffer 1X, once in FACS buffer and then proceed to data acquisition using BD FACSCanto II.

Immunocytochemistry

For immunofluorescence (IF) staining, cells were fixed in 4% PFA in PBS for 12 min at RT, permeabilized with 0.1% Triton X-100 for 10 mins (this step was not performed when staining dECMs) and blocked in PBS with 2,5% of bovine serum albumin (BSA, Biowest). After incubation with primary antibodies (Table 1), cells were incubated with the appropriate Alexa fluorochrome-conjugated secondary antibodies. Nuclei were counterstained with 4',6'-diamidino-2-phenylindole (DAPI). Samples were visualized with Zeiss LSM 780 confocal microscope.

RNA extraction and RT-PCR

Total RNA was extracted using a High Pure RNA Isolation Kit (Roche, Base, Switzerland) according to the manufacturer's instructions. Reverse transcription (1 µg of RNA) was performed using Transcription First Strand cDNA Synthesis Kit (Roche) and real-time qPCR was carried out in duplicate, using a LightCycler 480 SYBR Green I Master Kit (Roche) and run on a LightCycler 480 Real-Time PCR System (Roche). The expression level of individual genes was determined by ΔCt method relative to the expression of the housekeeping gene GAPDH. Primers used are shown in Table 2.

RNA Sequencing (RNA-seq) and Data Analysis

High-throughput RNA-Seq data were prepared using Lexogen QuantSeq 3' mRNA-Seq Library Prep Kit FWD for Illumina with polyA selection using 200 ng/µl of total RNA per sample as an input and sequenced on Illumina NextSeq 500 sequencer (run length 1 × 75 nt). Bcl files were converted to Fastq format using bcl2fastq v. 2.20.0.422 Illumina software for basecalling. Quality check of raw single-end fastq reads was carried out by FastQC v0.11.9 [60]. The adapters and quality trimming of raw fastq reads was performed using Trimmomatic v0.36 [61] with settings CROP:250 LEADING:3 TRAILING:3 SLIDINGWINDOW:4:5 MINLEN:35. Trimmed RNA-Seq reads were mapped against the human genome (hg38) and Ensembl GRCh38-p10 annotation using STAR v2.7.3a [62] as splice-aware short read aligner and default parameters except –outFilterMismatchNoverLmax 0.4 and –twopassMode Basic. Quality control after alignment concerning the number and percentage of uniquely and multi-mapped reads, rRNA contamination, mapped regions, read coverage distribution, strand specificity, gene biotypes and PCR duplication was performed using several tools namely RSeQC v4.0.0 [63], Picard toolkit v2.25.6 [64] and Qualimap v.2.2.2 [65]. The raw gene counts were produced using featureCounts from Subread package v2.0 [66]. Differential expression analysis was done using the Bioconductor package EdgeR v4.0.5, in which the previously filtered and normalized counts from all samples were fitted into negative binomial generalized linear models and then sample groups were compared using quasi-likelihood F-test [67-69]. Genes were considered differentially expressed based on a cut-off of adjusted p-value ≤ 0.05 and $\log_2$(fold-change) ≥1 or ≤−1.
2D and 3D PCA graphs were produced using the R package PCA tools v2.14.0 [70] and rgl v1.3.1 [71] and volcano plots were obtained using ggplot2 v3.4.4 [72] and ggrepel v0.9.4 [73]. The clustered heatmaps were generated using pheatmap v1.0.12 [74] and dotpots, barplots and other representations of GSEA and Reactome pathways were produced using the clusterProfiler v4.10.0 [75, 76], enrichplot v1.22.0 [77] and org.Hs.eg.db v3.18.0 [78]. Human matrisome analysis was done using MatrisomeAnalyzeR v1.0.1 [35, 79]. Gene networks were made using Cytoscape [80] and gene enrichment clustering was obtained using DAVID [81]. Predictive direct targets of YAP were obtained using the Harmonizome 3.0 database [82].

Western Blot

For total protein extraction, the cells were lysed in RIPA buffer (Merck Millipore, Burlington, MA, USA) supplemented with a protease and phosphatase inhibitor cocktail (1%, Sigma-Aldrich) on ice for 30 min and then centrifuged at 16,000 x g for 15 min at 4°C. Protein concentration was determined by BCA method (Thermo Fisher Scientific) with a spectrophotometer (Multiskan™ GO, Thermo Fisher Scientific) set at 562 nm using bovine serum albumin as standards. Protein samples were loaded in 10% polyacrylamide gels prepared using TGX™ FastCast™ Acrylamide Solutions (Bio-Rad, Hercules, CA, USA) and run at 80 V for 30 mins and 100V until the protein ladder were resolved. The proteins were transferred to a nitrocellulose membrane (Bio-Rad) using the Trans-Blot Turbo transfer system (Bio-Rad). Membranes were blocked with 5% BSA in TBS-T, incubated with diluted primary antibody (Table 1) in 5% BSA in TBS-T at 4°C with rotation overnight and then probed with the appropriate secondary HRP-conjugated antibody at room temperature for 1 h. Then, the blots were incubated for 1 minute with Clarity™ Western ECL Substrate (Bio-Rad) and ChemiDoc™ MP Imaging System (Bio-Rad) was used to detect chemiluminescence. The uncropped blots are available in Supplementary Figure 5.

Image analysis

The acquired images were processed using the following methods: **(1)** The percentage of GATA4 positive cells were calculated using Fiji-ImageJ [83] and Cell Profiler 4.2.6 [84] to count cell nuclei in YAP WT and KO CFbs; **(2)** To calculate focal adhesion number and area, Fiji-ImageJ [83] was used to first manually select individual cells and excluding the rest of the image, which was used to calculate cell area, the mean intensity of phospho-MLC2 and to isolate the cell to be analyzed. After that, a script was applied to every cell image stained for vinculin in which Auto Local Threshold was applied using the Phansalkar method with a radius of 20 pixels, followed by the Despeckle and Watershed functions to make the focal adhesions more prominent. After this, the Analyze Particles function was used to measure focal adhesions with size between 0.3 and 25 μm^2, to clear possible noise from the measurement. As a further correction, images with overlays of the measured particles were used to exclude false positives; **(3)** The 2D field of local orientation θ of both phase contrast images of cells and confocal images of the ECM and actin, was extracted by using the Fiji plugin OrientationJ, based on the structure tensor method[85]. This tool allowed us to extract the local orientation vectors corresponding to image intensity sub-windows of cells, ECM or actin. The amplitude of these orientation vectors, named coherency, was also extracted from the imageJ plugin OrientationJ and is referred to as Anisotropy in this manuscript. Orientation vector fields and anisotropy maps in figures were represented with Matlab. The order parameter $Q = \sqrt{\langle \cos 2\,\theta \rangle^2_{x,y\in\omega} + \langle \sin 2\,\theta \rangle^2_{x,y\in\omega}}$ was calculated for spatial windows ω, with custom-made codes in Matlab. To extract nuclei orientation, we used the built-in Fiji functions Analyse particles from binarized confocal images. Statistical analysis of the comparisons of nuclei, F-actin and fibronectin orientations was done using the circular R package [86]. Finally, the normalized spatial nematic autocorrelation function was calculated from each orientational field position like $C_{nn}(\delta) = 2\left(\left\langle \cos^2\left(\theta(r) - \theta(r+\delta)\right)\right\rangle - 0.5\right)$. By fitting these data to single exponential functions $y = e^{-\frac{r}{\delta_{nn}}}$, we could quantify the characteristic autocorrelation lengths δ_{nn}; **(4)** dECM matrix coverage and mean intensity was obtained by using Fiji-ImageJ [83] applying Auto Thresholding using Li's Minimum Cross Entropy thresholding method to obtain a covered area and mean intensity of each stained protein. **(5)** ECM alignment was obtained using the TWOMBLI macro [39], using the following parameters: Contrast Saturation 0.35, Min and Max Line width 25, Min and Max Curvature Window 50, Min Branch Length 15, Maximum display HDM 225 for images obtained in control conditions and Contrast Saturation 0.35, Min and Max Line width 20, Min and Max Curvature Window 50, Min Branch Length 10, Maximum display HDM 220 for images obtained in activation conditions; **(6)** Densiometric data obtained in ChemiDoc™ MP Imaging System was analyzed using the Image Lab 6.0.1 software.

CRediT authorship contribution statement

Daniel Pereira-Sousa: Writing - original draft, Methodology, Investigation, Formal Analysis, Software, Data Curation. **Pau Guillamat:** Writing - original draft, Methodology, Conceptualization, Formal analysis, Software, Resources. **Francesco Niro:** Resources, Methodology, Formal analysis. **Vladimír Vinarský:** Software, Resources. **Soraia Fernandes:** Supervision, Writing - review & editing. **Marco Cassani:** Supervision, Writing - review & editing. **Stefania Pagliari:** Supervision, Methodology, Resources. **Xavier Trepat:** Supervision, Resources. **Marco Rasponi:** Supervision, Funding acquisition. **Jorge Oliver-De La Cruz:** Writing - original

draft, Supervision, Methodology, Formal analysis, Conceptualization. **Giancarlo Forte:** Supervision, Conceptualization, Funding acquisition, Writing - original draft, Writing - review & editing.

Data and code availability

All data generated during this study are available upon request from the corresponding authors.

Acknowledgements

This project has received funding from the European Union's Horizon 2020 research and innovation programme under the Marie Skłodowska-Curie grant agreement No 860715 and by Marie Curie H2020-MSCA-IF-2020 MSCA-IF-GF "MecHA-Nano", Grant Agreement No 101031744. We thank the Genomics and Bioinformatics Core Facilities of CEITEC Masaryk University for their support with data analysis and statistics. We are thankful to Helena Ďuríková for helping with cell culture, Romana Vlčková and Hana Dulová for the continuous technical support. P.G. acknowledges support from the European Union's Horizon 2020 Europe Research and Innovation programme under the Marie Skłodowska-Curie grant agreement No 101065794.

Declaration of interest

The authors declare no conflict of interests.

References

[1] N.R. Tucker, M. Chaffin, S.J. Fleming, A.W. Hall, V.A. Parsons, K.C. Bedi, Jr., A.D. Akkad, C.N. Herndon, A. Arduini, I. Papangeli, C. Roselli, F. Aguet, S.H. Choi, K.G. Ardlie, M. Babadi, K.B. Margulies, C.M. Stegmann, P.T. Ellinor, Transcriptional and Cellular Diversity of the Human Heart, Circulation 142(5) (2020) 466-482.

[2] J. Yu, M.M. Seldin, K. Fu, S. Li, L. Lam, P. Wang, Y. Wang, D. Huang, T.L. Nguyen, B. Wei, R.P. Kulkarni, D. Di Carlo, M. Teitell, M. Pellegrini, A.J. Lusis, A. Deb, Topological Arrangement of Cardiac Fibroblasts Regulates Cellular Plasticity, Circ Res 123(1) (2018) 73-85.

[3] E.N. Farah, R.K. Hu, C. Kern, Q. Zhang, T.-Y. Lu, Q. Ma, S. Tran, B. Zhang, D. Carlin, A. Monell, A.P. Blair, Z. Wang, J. Eschbach, B. Li, E. Destici, B. Ren, S.M. Evans, S. Chen, Q. Zhu, N.C. Chi, Spatially organized cellular communities form the developing human heart, Nature 627(8005) (2024) 854-864.

[4] V. Talman, H. Ruskoaho, Cardiac fibrosis in myocardial infarction-from repair and remodeling to regeneration, Cell Tissue Res 365(3) (2016) 563-81.

[5] A. Ruiz-Villalba, A.M. Simón, C. Pogontke, M.I. Castillo, G. Abizanda, B. Pelacho, R. Sánchez-Domínguez, J.C. Segovia, F. Prósper, J.M. Pérez-Pomares, Interacting resident epicardium-derived fibroblasts and recruited bone marrow cells form myocardial infarction scar, J Am Coll Cardiol 65(19) (2015) 2057-66.

[6] J.B. Caulfield, T.K. Borg, The collagen network of the heart, Lab Invest 40(3) (1979) 364-72.

[7] K.D. Dwyer, K.L.K. Coulombe, Cardiac mechanostructure: Using mechanics and anisotropy as inspiration for developing epicardial therapies in treating myocardial infarction, Bioactive Materials 6(7) (2021) 2198-2220.

[8] M. Pesce, G.N. Duda, G. Forte, H. Girao, A. Raya, P. Roca-Cusachs, J.P.G. Sluijter, C. Tschöpe, S. Van Linthout, Cardiac fibroblasts and mechanosensation in heart development, health and disease, Nature Reviews Cardiology 20(5) (2023) 309-324.

[9] J. Francisco, Y. Zhang, Y. Nakada, J.I. Jeong, C.Y. Huang, A. Ivessa, S. Oka, G.J. Babu, D.P. Del Re, AAV-mediated YAP expression in cardiac fibroblasts promotes inflammation and increases fibrosis, Sci Rep 11(1) (2021) 10553.

[10] M. Liu, B. Lopez de Juan Abad, K. Cheng, Cardiac fibrosis: Myofibroblast-mediated pathological regulation and drug delivery strategies, Adv Drug Deliv Rev 173 (2021) 504-519.

[11] B.L. Brazile, J.R. Butler, S.S. Patnaik, A. Claude, R. Prabhu, L.N. Williams, K.L. Perez, K.T. Nguyen, G. Zhang, P. Bajona, M. Peltz, Y. Yang, Y. Hong, J. Liao, Biomechanical properties of acellular scar ECM during the acute to chronic stages of myocardial infarction, Journal of the Mechanical Behavior of Biomedical Materials 116 (2021) 104342.

[12] J. Luo, P. Li, Context-dependent transcriptional regulations of YAP/TAZ in stem cell and differentiation, Stem Cell Res Ther 13(1) (2022) 10.

[13] H. Zhang, H.A. Pasolli, E. Fuchs, Yes-associated protein (YAP) transcriptional coactivator functions in balancing growth and differentiation in skin, Proc Natl Acad Sci U S A 108(6) (2011) 2270-5.

[14] S. Piccolo, S. Dupont, M. Cordenonsi, The biology of YAP/TAZ: hippo signaling and beyond, Physiol Rev 94(4) (2014) 1287-312.

[15] A. Totaro, T. Panciera, S. Piccolo, YAP/TAZ upstream signals and downstream responses, Nat Cell Biol 20(8) (2018) 888-899.

[16] S. Ma, Z. Meng, R. Chen, K.L. Guan, The Hippo Pathway: Biology and Pathophysiology, Annu Rev Biochem 88 (2019) 577-604.

[17] F. Martino, A.R. Perestrelo, V. Vinarský, S. Pagliari, G. Forte, Cellular Mechanotransduction: From Tension to Function, Front Physiol 9 (2018) 824.

[18] E.M. Morin-Kensicki, B.N. Boone, M. Howell, J.R. Stonebraker, J. Teed, J.G. Alb, T.R. Magnuson, W. O'Neal, S.L. Milgram, Defects in yolk sac vasculogenesis, chorioallantoic fusion,

and embryonic axis elongation in mice with targeted disruption of Yap65, Mol Cell Biol 26(1) (2006) 77-87.
[19] A. von Gise, Z. Lin, K. Schlegelmilch, L.B. Honor, G.M. Pan, J.N. Buck, Q. Ma, T. Ishiwata, B. Zhou, F.D. Camargo, W.T. Pu, YAP1, the nuclear target of Hippo signaling, stimulates heart growth through cardiomyocyte proliferation but not hypertrophy, Proc Natl Acad Sci U S A 109(7) (2012) 2394-9.
[20] M. Sharifi-Sanjani, M. Berman, D. Goncharov, M. Alhamaydeh, T.G. Avolio, J. Baust, B. Chang, A. Kobir, M. Ross, C. St Croix, S.M. Nouraie, C.F. McTiernan, C.S. Moravec, E. Goncharova, I. Al Ghouleh, Yes-Associated Protein (Yap) Is Up-Regulated in Heart Failure and Promotes Cardiac Fibroblast Proliferation, Int J Mol Sci 22(11) (2021).
[21] A. Mondal, S. Das, J. Samanta, S. Chakraborty, A. Sengupta, YAP1 induces hyperglycemic stress-mediated cardiac hypertrophy and fibrosis in an AKT-FOXM1 dependent signaling pathway, Arch Biochem Biophys 722 (2022) 109198.
[22] B. Jin, J. Zhu, H.M. Shi, Z.C. Wen, B.W. Wu, YAP activation promotes the transdifferentiation of cardiac fibroblasts to myofibroblasts in matrix remodeling of dilated cardiomyopathy, Braz J Med Biol Res 52(1) (2018) e7914.
[23] G. Garoffolo, M. Casaburo, F. Amadeo, M. Salvi, G. Bernava, L. Piacentini, I. Chimenti, G. Zaccagnini, G. Milcovich, E. Zuccolo, M. Agrifoglio, S. Ragazzini, O. Baasansuren, C. Cozzolino, M. Chiesa, S. Ferrari, D. Carbonaro, R. Santoro, M. Manzoni, L. Casalis, A. Raucci, F. Molinari, L. Menicanti, F. Pagano, T. Ohashi, F. Martelli, D. Massai, G.I. Colombo, E. Messina, U. Morbiducci, M. Pesce, Reduction of Cardiac Fibrosis by Interference With YAP-Dependent Transactivation, Circ Res 131(3) (2022) 239-257.
[24] S. Ragazzini, F. Scocozza, G. Bernava, F. Auricchio, G.I. Colombo, M. Barbuto, M. Conti, M. Pesce, G. Garoffolo, Mechanosensor YAP cooperates with TGF-beta1 signaling to promote myofibroblast activation and matrix stiffening in a 3D model of human cardiac fibrosis, Acta Biomater 152 (2022) 300-312.
[25] E.M. Small, A.C. Brooks, Cut the YAP: Limiting Fibrosis in Pathologic Cardiac Remodeling, JACC Basic Transl Sci 5(9) (2020) 946-948.
[26] D. Bugg, R. Bretherton, P. Kim, E. Olszewski, A. Nagle, A.E. Schumacher, N. Chu, J. Gunaje, C.A. DeForest, K. Stevens, D.H. Kim, J. Davis, Infarct Collagen Topography Regulates Fibroblast Fate via p38-Yes-Associated Protein Transcriptional Enhanced Associate Domain Signals, Circ Res 127(10) (2020) 1306-1322.
[27] A.R. Perestrelo, A.C. Silva, J. Oliver-De La Cruz, F. Martino, V. Horváth, G. Caluori, O. Polanský, V. Vinarský, G. Azzato, G. de Marco, V. Žampachová, P. Skládal, S. Pagliari, A. Rainer, P. Pinto-do-Ó, A. Caravella, K. Koci, D.S. Nascimento, G. Forte, Multiscale Analysis of Extracellular Matrix Remodeling in the Failing Heart, Circ Res 128(1) (2021) 24-38.
[28] T.B. Saw, W. Xi, B. Ladoux, C.T. Lim, Biological Tissues as Active Nematic Liquid Crystals, Adv Mater 30(47) (2018) e1802579.
[29] J. Zhang, R. Tao, K.F. Campbell, J.L. Carvalho, E.C. Ruiz, G.C. Kim, E.G. Schmuck, A.N. Raval, A.M. da Rocha, T.J. Herron, J. Jalife, J.A. Thomson, T.J. Kamp, Functional cardiac fibroblasts derived from human pluripotent stem cells via second heart field progenitors, Nature Communications 10(1) (2019) 2238.
[30] M. Litviňuková, C. Talavera-López, H. Maatz, D. Reichart, C.L. Worth, E.L. Lindberg, M. Kanda, K. Polanski, M. Heinig, M. Lee, E.R. Nadelmann, K. Roberts, L. Tuck, E.S. Fasouli, D.M. DeLaughter, B. McDonough, H. Wakimoto, J.M. Gorham, S. Samari, K.T. Mahbubani, K. Saeb-Parsy, G. Patone, J.J. Boyle, H. Zhang, H. Zhang, A. Viveiros, G.Y. Oudit, O.A. Bayraktar, J.G. Seidman, C.E. Seidman, M. Noseda, N. Hubner, S.A. Teichmann, Cells of the adult human heart, Nature 588(7838) (2020) 466-472.
[31] M.B. Furtado, M.W. Costa, E.A. Pranoto, E. Salimova, A.R. Pinto, N.T. Lam, A. Park, P. Snider, A. Chandran, R.P. Harvey, R. Boyd, S.J. Conway, J. Pearson, D.M. Kaye, N.A. Rosenthal, Cardiogenic Genes Expressed in Cardiac Fibroblasts Contribute to Heart Development and Repair, Circulation Research 114(9) (2014) 1422-1434.

[32] N. Huebsch, Collective organization from cellular disorder, Biophysical Journal 121(22) (2022) 4239-4241.
[33] G. Duclos, S. Garcia, H.G. Yevick, P. Silberzan, Perfect nematic order in confined monolayers of spindle-shaped cells, Soft Matter 10(14) (2014) 2346-2353.
[34] S. Dupont, L. Morsut, M. Aragona, E. Enzo, S. Giulitti, M. Cordenonsi, F. Zanconato, J. Le Digabel, M. Forcato, S. Bicciato, N. Elvassore, S. Piccolo, Role of YAP/TAZ in mechanotransduction, Nature 474(7350) (2011) 179-183.
[35] A. Naba, K.R. Clauser, S. Hoersch, H. Liu, S.A. Carr, R.O. Hynes, The matrisome: in silico definition and in vivo characterization by proteomics of normal and tumor extracellular matrices, Mol Cell Proteomics 11(4) (2012) M111.014647.
[36] L. Li, Q. Zhao, W. Kong, Extracellular matrix remodeling and cardiac fibrosis, Matrix Biology 68-69 (2018) 490-506.
[37] N.G. Frangogiannis, The Extracellular Matrix in Ischemic and Nonischemic Heart Failure, Circulation Research 125(1) (2019) 117-146.
[38] F. Niro, S. Fernandes, M. Cassani, M. Apostolico, J.O. Cruz, D. Pereira-Sousa, S. Pagliari, V. Vinarsky, Z. Zdráhal, D. Potesil, V. Pustka, G. Pompilio, E. Sommariva, D. Rovina, A.S. Maione, L. Bersanini, M. Becker, M. Rasponi, G. Forte, Fibrotic extracellular matrix impacts cardiomyocyte phenotype and function in an iPSC-derived isogenic model of cardiac fibrosis, Transl Res (2024).
[39] E. Wershof, D. Park, D.J. Barry, R.P. Jenkins, A. Rullan, A. Wilkins, K. Schlegelmilch, I. Roxanis, K.I. Anderson, P.A. Bates, E. Sahai, A FIJI macro for quantifying pattern in extracellular matrix, Life Science Alliance 4(3) (2021) e202000880.
[40] J.T. Parsons, A.R. Horwitz, M.A. Schwartz, Cell adhesion: integrating cytoskeletal dynamics and cellular tension, Nat Rev Mol Cell Biol 11(9) (2010) 633-43.
[41] J.C. Kuo, Mechanotransduction at focal adhesions: integrating cytoskeletal mechanics in migrating cells, J Cell Mol Med 17(6) (2013) 704-12.
[42] G. Nardone, J. Oliver-De La Cruz, J. Vrbsky, C. Martini, J. Pribyl, P. Skládal, M. Pešl, G. Caluori, S. Pagliari, F. Martino, Z. Maceckova, M. Hajduch, A. Sanz-Garcia, N.M. Pugno, G.B. Stokin, G. Forte, YAP regulates cell mechanics by controlling focal adhesion assembly, Nat Commun 8 (2017) 15321.
[43] S. Pagliari, V. Vinarsky, F. Martino, A.R. Perestrelo, J. Oliver De La Cruz, G. Caluori, J. Vrbsky, P. Mozetic, A. Pompeiano, A. Zancla, S.G. Ranjani, P. Skladal, D. Kytyr, Z. Zdráhal, G. Grassi, M. Sampaolesi, A. Rainer, G. Forte, YAP–TEAD1 control of cytoskeleton dynamics and intracellular tension guides human pluripotent stem cell mesoderm specification, Cell Death & Differentiation 28(4) (2021) 1193-1207.
[44] A.D. Doyle, S.S. Nazari, K.M. Yamada, Cell-extracellular matrix dynamics, Phys Biol 19(2) (2022).
[45] P. Bordignon, G. Bottoni, X. Xu, A.S. Popescu, Z. Truan, E. Guenova, L. Kofler, P. Jafari, P. Ostano, M. Röcken, V. Neel, G.P. Dotto, Dualism of FGF and TGF-β Signaling in Heterogeneous Cancer-Associated Fibroblast Activation with ETV1 as a Critical Determinant, Cell Rep 28(9) (2019) 2358-2372.e6.
[46] F. Liu, D. Lagares, K.M. Choi, L. Stopfer, A. Marinković, V. Vrbanac, C.K. Probst, S.E. Hiemer, T.H. Sisson, J.C. Horowitz, I.O. Rosas, L.E. Fredenburgh, C. Feghali-Bostwick, X. Varelas, A.M. Tager, D.J. Tschumperlin, Mechanosignaling through YAP and TAZ drives fibroblast activation and fibrosis, American Journal of Physiology-Lung Cellular and Molecular Physiology 308(4) (2015) L344-L357.
[47] D. Park, E. Wershof, S. Boeing, A. Labernadie, R.P. Jenkins, S. George, X. Trepat, P.A. Bates, E. Sahai, Extracellular matrix anisotropy is determined by TFAP2C-dependent regulation of cell collisions, Nat Mater 19(2) (2020) 227-238.
[48] S.C. Dinca, D. Greiner, K. Weidenfeld, L. Bond, D. Barkan, C.L. Jorcyk, Novel mechanism for OSM-promoted extracellular matrix remodeling in breast cancer: LOXL2 upregulation and subsequent ECM alignment, Breast Cancer Research 23(1) (2021) 56.

[49] X. Li, R. Balagam, T.-F. He, P.P. Lee, O.A. Igoshin, H. Levine, On the mechanism of long-range orientational order of fibroblasts, Proceedings of the National Academy of Sciences 114(34) (2017) 8974-8979.
[50] C. Jacques, J. Ackermann, S. Bell, C. Hallopeau, C.P.-. Gonzalez, L. Balasubramaniam, X. Trepat, B. Ladoux, A. Maitra, R. Voituriez, D.M. Vignjevic, Aging and freezing of active nematic dynamics of cancer-associated fibroblasts by fibronectin matrix remodeling, bioRxiv (2023) 2023.11.22.568216.
[51] D.J. Glenn, D. Rahmutula, M. Nishimoto, F. Liang, D.G. Gardner, Atrial natriuretic peptide suppresses endothelin gene expression and proliferation in cardiac fibroblasts through a GATA4-dependent mechanism, Cardiovasc Res 84(2) (2009) 209-17.
[52] P. Umbarkar, S. Ejantkar, S. Tousif, H. Lal, Mechanisms of Fibroblast Activation and Myocardial Fibrosis: Lessons Learned from FB-Specific Conditional Mouse Models, Cells 10(9) (2021).
[53] B. Zhao, X. Ye, J. Yu, L. Li, W. Li, S. Li, J. Yu, J.D. Lin, C.Y. Wang, A.M. Chinnaiyan, Z.C. Lai, K.L. Guan, TEAD mediates YAP-dependent gene induction and growth control, Genes Dev 22(14) (2008) 1962-71.
[54] S.W. Plouffe, K.C. Lin, J.L. Moore, F.E. Tan, S. Ma, Z. Ye, Y. Qiu, B. Ren, K.-L. Guan, The Hippo pathway effector proteins YAP and TAZ have both distinct and overlapping functions in the cell, Journal of Biological Chemistry 293(28) (2018) 11230-11240.
[55] M.M. Chen, A. Lam, J.A. Abraham, G.F. Schreiner, A.H. Joly, CTGF expression is induced by TGF- beta in cardiac fibroblasts and cardiac myocytes: a potential role in heart fibrosis, J Mol Cell Cardiol 32(10) (2000) 1805-19.
[56] W. Luo, Y. Li, Y. Zeng, Y. Li, M. Cheng, C. Zhang, F. Li, Y. Wu, C. Huang, X. Yang, J. Kremerskothen, J. Zhang, C. Zhang, S. Tu, Z. Li, Z. Luo, Z. Lin, X. Yan, Tea domain transcription factor TEAD4 mitigates TGF-β signaling and hepatocellular carcinoma progression independently of YAP, J Mol Cell Biol 15(2) (2023).
[57] M.Z. Miranda, J.F. Bialik, P. Speight, Q. Dan, T. Yeung, K. Szászi, S.F. Pedersen, A. Kapus, TGF-β1 regulates the expression and transcriptional activity of TAZ protein via a Smad3-independent, myocardin-related transcription factor-mediated mechanism, J Biol Chem 292(36) (2017) 14902-14920.
[58] H. Qin, M. Hejna, Y. Liu, M. Percharde, M. Wossidlo, L. Blouin, J. Durruthy-Durruthy, P. Wong, Z. Qi, J. Yu, Lei S. Qi, V. Sebastiano, Jun S. Song, M. Ramalho-Santos, YAP Induces Human Naive Pluripotency, Cell Reports 14(10) (2016) 2301-2312.
[59] J.C. Shicheng Su, Collagen Gel Contraction Assay, Protocol Exchange (2015).
[60] S. Andrews, FastQC: a quality control tool for high throughput sequence data, Babraham Bioinformatics, Babraham Institute, Cambridge, United Kingdom, 2010.
[61] A.M. Bolger, M. Lohse, B. Usadel, Trimmomatic: a flexible trimmer for Illumina sequence data, Bioinformatics 30(15) (2014) 2114-2120.
[62] A. Dobin, C.A. Davis, F. Schlesinger, J. Drenkow, C. Zaleski, S. Jha, P. Batut, M. Chaisson, T.R. Gingeras, STAR: ultrafast universal RNA-seq aligner, Bioinformatics 29(1) (2012) 15-21.
[63] L. Wang, S. Wang, W. Li, RSeQC: quality control of RNA-seq experiments, Bioinformatics 28(16) (2012) 2184-2185.
[64] Picard toolkit, Broad Institute.
[65] J. Chu, S. Sadeghi, A. Raymond, S.D. Jackman, K.M. Nip, R. Mar, H. Mohamadi, Y.S. Butterfield, A.G. Robertson, I. Birol, BioBloom tools: fast, accurate and memory-efficient host species sequence screening using bloom filters, Bioinformatics 30(23) (2014) 3402-3404.
[66] Y. Liao, G.K. Smyth, W. Shi, featureCounts: an efficient general purpose program for assigning sequence reads to genomic features, Bioinformatics 30(7) (2013) 923-930.
[67] Y. Chen, A. Lun, G. Smyth, From reads to genes to pathways: differential expression analysis of RNA-Seq experiments using Rsubread and the edgeR quasi-likelihood pipeline [version 2; peer review: 5 approved], F1000Research 5(1438) (2016).

[68] D.J. McCarthy, Y. Chen, G.K. Smyth, Differential expression analysis of multifactor RNA-Seq experiments with respect to biological variation, Nucleic Acids Research 40(10) (2012) 4288-4297.
[69] M.D. Robinson, D.J. McCarthy, G.K. Smyth, edgeR: a Bioconductor package for differential expression analysis of digital gene expression data, Bioinformatics 26(1) (2009) 139-140.
[70] K. Blighe, A. Lun, PCAtools: PCAtools: Everything Principal Components Analysis, (2023).
[71] D. Murdoch, D. Adler, rgl: 3D Visualization Using OpenGL, (2024).
[72] H. Wickham, ggplot2: Elegant Graphics for Data Analysis, (2016).
[73] K. Slowikowski, ggrepel: Automatically Position Non-Overlapping Text Labels with 'ggplot2', (2024).
[74] R. Kolde, pheatmap: Pretty Heatmaps, (2019).
[75] T. Wu, E. Hu, S. Xu, M. Chen, P. Guo, Z. Dai, T. Feng, L. Zhou, W. Tang, L. Zhan, X. Fu, S. Liu, X. Bo, G. Yu, clusterProfiler 4.0: A universal enrichment tool for interpreting omics data, The Innovation 2(3) (2021).
[76] G. Yu, L.-G. Wang, Y. Han, Q.-Y. He, clusterProfiler: an R Package for Comparing Biological Themes Among Gene Clusters, OMICS: A Journal of Integrative Biology 16(5) (2012) 284-287.
[77] G. Yu, enrichplot: Visualization of Functional Enrichment Result, (2023).
[78] M. Carlson, org.Hs.eg.db: Genome wide annotation for Human, (2023).
[79] P.B. Petrov, J.M. Considine, V. Izzi, A. Naba, Matrisome AnalyzeR - a suite of tools to annotate and quantify ECM molecules in big datasets across organisms, J Cell Sci 136(17) (2023).
[80] P. Shannon, A. Markiel, O. Ozier, N.S. Baliga, J.T. Wang, D. Ramage, N. Amin, B. Schwikowski, T. Ideker, Cytoscape: a software environment for integrated models of biomolecular interaction networks, Genome Res 13(11) (2003) 2498-504.
[81] D.W. Huang, B.T. Sherman, R.A. Lempicki, Systematic and integrative analysis of large gene lists using DAVID bioinformatics resources, Nature Protocols 4(1) (2009) 44-57.
[82] A.D. Rouillard, G.W. Gundersen, N.F. Fernandez, Z. Wang, C.D. Monteiro, M.G. McDermott, A. Ma'ayan, The harmonizome: a collection of processed datasets gathered to serve and mine knowledge about genes and proteins, Database 2016 (2016).
[83] J. Schindelin, I. Arganda-Carreras, E. Frise, V. Kaynig, M. Longair, T. Pietzsch, S. Preibisch, C. Rueden, S. Saalfeld, B. Schmid, J.-Y. Tinevez, D.J. White, V. Hartenstein, K. Eliceiri, P. Tomancak, A. Cardona, Fiji: an open-source platform for biological-image analysis, Nature Methods 9(7) (2012) 676-682.
[84] D.R. Stirling, M.J. Swain-Bowden, A.M. Lucas, A.E. Carpenter, B.A. Cimini, A. Goodman, CellProfiler 4: improvements in speed, utility and usability, BMC Bioinformatics 22(1) (2021) 433.
[85] Z. Püspöki, M. Storath, D. Sage, M. Unser, Transforms and Operators for Directional Bioimage Analysis: A Survey, Adv Anat Embryol Cell Biol 219 (2016) 69-93.
[86] C. Agostinelli, U. Lund, R package circular: Circular Statistics (version 0.5-1), (2024).

TABLES

Table 1 - List of antibodies used.				
Method	**Target protein**	**Dilution**	**Catalog No.**	**Manufacturer**
IF	YAP	1:100	4912	Cell Signalling
	GATA4	1:400	36966	Cell Signalling
	Vinculin	1:400	V9131	Sigma-Aldrich
	Phospho-MLC2	1:150	3671	Cell Signalling
	α-SMA	1:100	ab7817	Abcam
	Collagen 1	1:100	600-401-103	Rockland
	Fibronectin	1:100	F0791	Sigma-Aldrich
	Collagen 4	1:50	AB769	Millipore
	Alexa Fluor™ 488 Donkey anti-mouse IgG	1:500	A21202	Invitrogen
	Alexa Fluor™ 555 Donkey anti-rabbit IgG	1:500	A31572	Invitrogen
	Alexa Fluor™ 546 Goat anti-mouse IgG	1:500	A11030	Invitrogen
	Alexa Fluor™ 647 Donkey anti-goat IgG	1:500	A21447	Invitrogen
	Alexa Fluor™ 647 Goat anti-rabbit IgG	1:500	A21245	Invitrogen
	Alexa Fluor™ 488 Phalloidin	1:200	A12379	Invitrogen
	Alexa Fluor™ 555 Phalloidin	1:200	A34055	Invitrogen
FC	CD31-FITC	1:20	11-0311-82	ThermoFisher
	CD90-APC	1:10	1A-625-T100	Exbio
	CD45-APC	1:10	17-0451082	ThermoFisher
	CD73-FITC	1:10	41-0200	ThermoFisher
	α-SMA-FITC	1:10	Ab7817	Abcam
	CD105-PE	1:20	12-1057-42	Invitrogen
	CD146-E450	1:20	48-1469-42	Invitrogen
	FAP-APC	1:10	FAP3715A	RnD Systems
WB	Phospho-MLC2	1:1000	3671	Cell Signalling
	MLC2	1:1000	ab79935	Abcam
	YAP	1:1000	14074	Cell Signalling
	Phospho-ERM	1:1000	3149P	Cell Signalling
	ERM	1:1000	3142P	Cell Signalling
	Phospho-FAK	1:1000	8556T	Cell Signalling
	FAK	1:1000	13009T	Cell Signalling
	Phospho-VASP	1:1000	3114P	Cell Signalling
	VASP	1:1000	3132P	Cell Signalling
	GAPDH-HRP	1:5000	G9295	Sigma-Aldrich
	Anti-rabbit HRP	1:2000	7074P2	Cell Signalling
	Anti-mouse HRP	1:2000	A16017	Invitrogen

Table 2 - List of primers used.		
Gene	**Forward sequence**	**Reverse sequence**
GATA4	GCCACTACCTGTGCAACGCCT	CAATCCAAGCCGCCGTGATGAA
NKX2-5	AAGTGTGCGTCTGCCTTTCCCG	TTGTCCGCCTCTGTCTTCTCCA
WT1	CGAGAGCGATAACCACACAACG	GTCTCAGATCGATAACCACGTACAA
α-SMA	CTATGCCTCTGGACGCACAACT	CAGATCCAGACGCATGATGGCA
COL1A1	GATTCCCTGGACCTAAAGGTGC	AGCCTCTCCATCTTTGCCAGCA
COL3A1	TAAAGGCGAAATGGGTCCCG	GGCACCATTCTTACCAGGCT
CNN2	AGGTAGGAAATGTGGTAGCC	AACAAATGCTTCCAGGTGAA
GAPDH	GTCTCCTCTGACTTCAACAGCG	ACCACCCTGTTGCTGTAGCCAA

Supplementary Figures

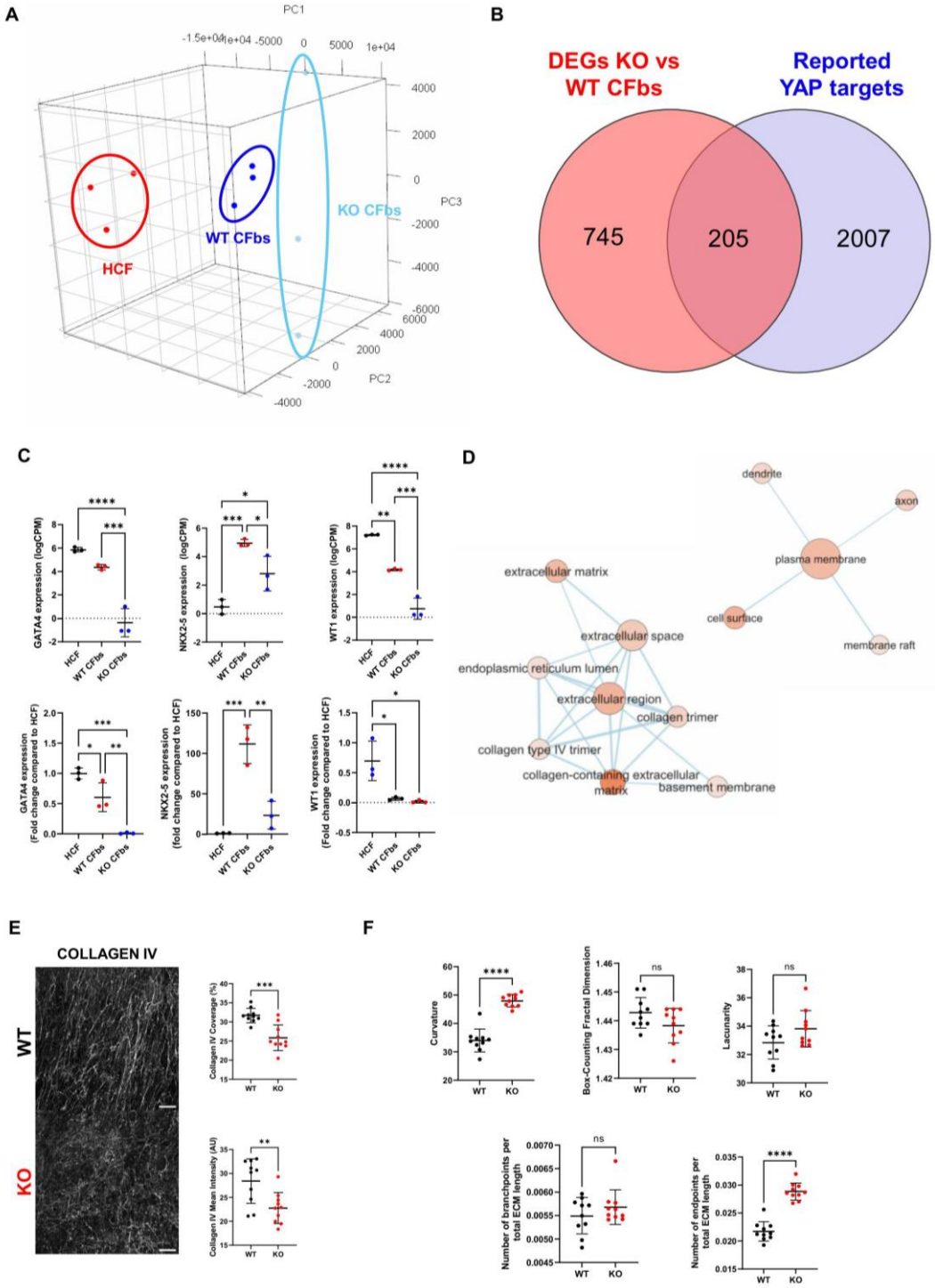

Supplementary Figure 1. Impact of YAP depletion in the gene expression and ECM deposition of CFbs. (A) 3D visualization of principal component analysis of global gene expression obtained by bulk RNASeq of WT and YAP KO CFbs together with adult primary cell line of human cardiac fibroblasts (HCF) (YAP WT/KO CFbs N=3; HCF N=3). **(B)** Veen diagram showing the intersection between DEGs obtained between YAP KO vs WT CFbs and reported direct targets of YAP obtained in Harmonizome 3.0 database[82]. **(C)** Dotplots of GATA4, NKX2-5 and WT1 expression obtained using the RNA sequencing (top) and RT-PCR (bottom) (YAP WT/KO CFbs N=3). Statistical analysis performed by ordinary one-way ANOVA, followed by Tukey's multiple comparisons test. **(D)** DAVID enrichment analysis results in which the nodes represent GO_CC terms. The size of the node represents the gene count in the respective term and the color represents -log(adjusted p-value). Data visualization was done using Cytoscape. **(E)** Dotplots of the coverage

and mean intensity of collagen IV in YAP WT and KO CFbs in control conditions (YAP WT/KO CFbs N=3). Statistical analysis performed by unpaired t-test. **(F)** Dotplots of hyphal growth unit (HGU), Box-counting fractal dimension, lacunarity, curvature and number of branchpoints and endpoints per ECM length obtained from dECM from YAP WT and KO CFbs. Statistical analysis performed by unpaired t test.

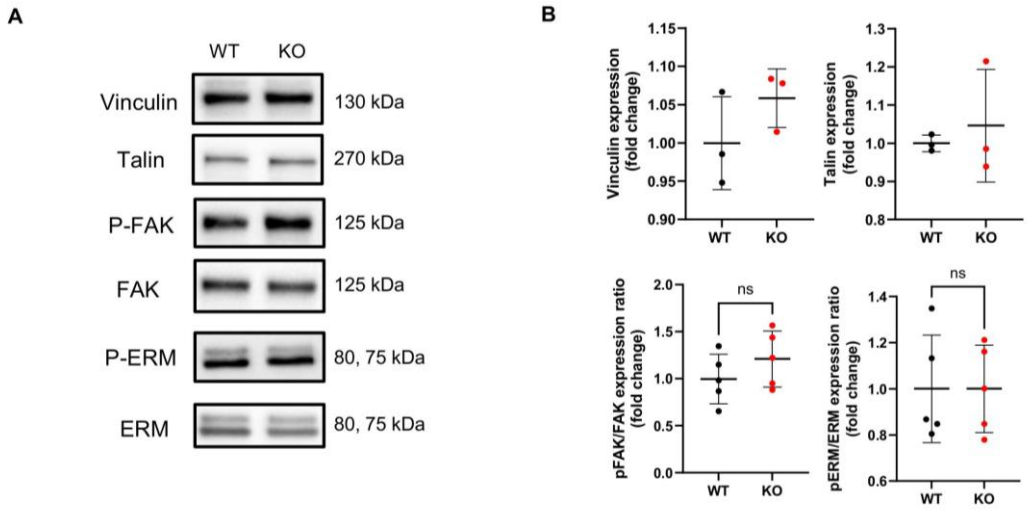

Supplementary Figure 2. Effect of YAP depletion on the expression and functionality of focal adhesion related proteins. (A) Representative blots of vinculin, talin, phospho- and total FAK and phospho- and total ERM in YAP WT and KO CFbs. **(B)** Dotplots of the quantification of the expression of vinculin and talin (N=3), and ratio of expression of phospho and total FAK and ERM (N=5) in YAP WT and KO CFbs. Statistical analysis performed by unpaired t test.

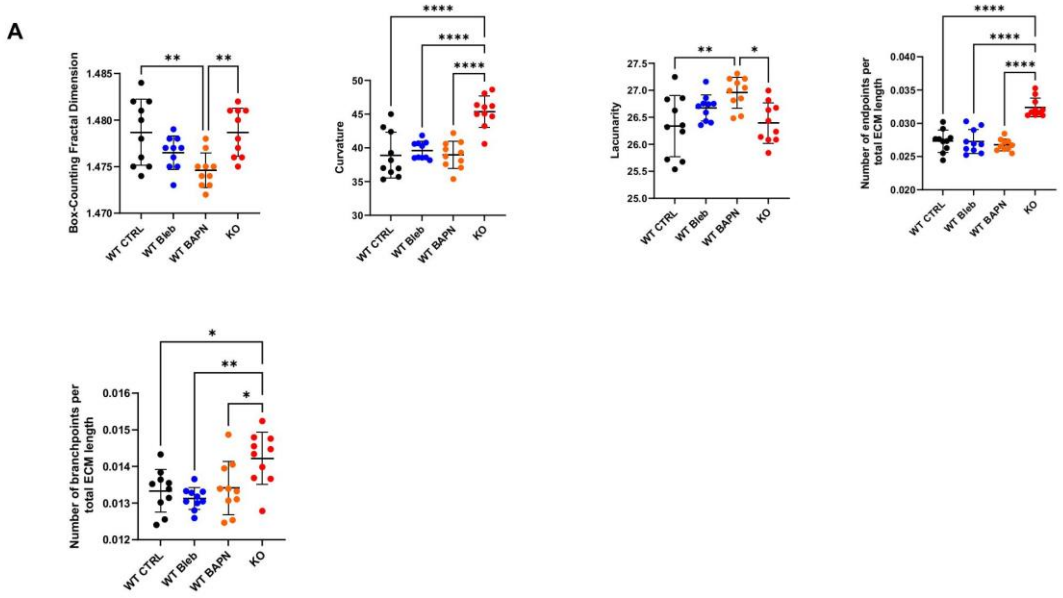

Supplementary Figure 3. Characterization of the ECM deposited by treated and non-treated WT CFbs and YAP KO CFbs. (A) Dotplots of Box-counting fractal dimension, lacunarity, curvature and number of branchpoints and endpoints per ECM length obtained from dECM from YAP WT CFbs, YAP WT CFbs treated with Blebbistatin, YAP WT CFbs treated with BAPN and KO CFbs. Statistical analysis performed by One-way ANOVA, followed by Tukey's multiple comparisons test.

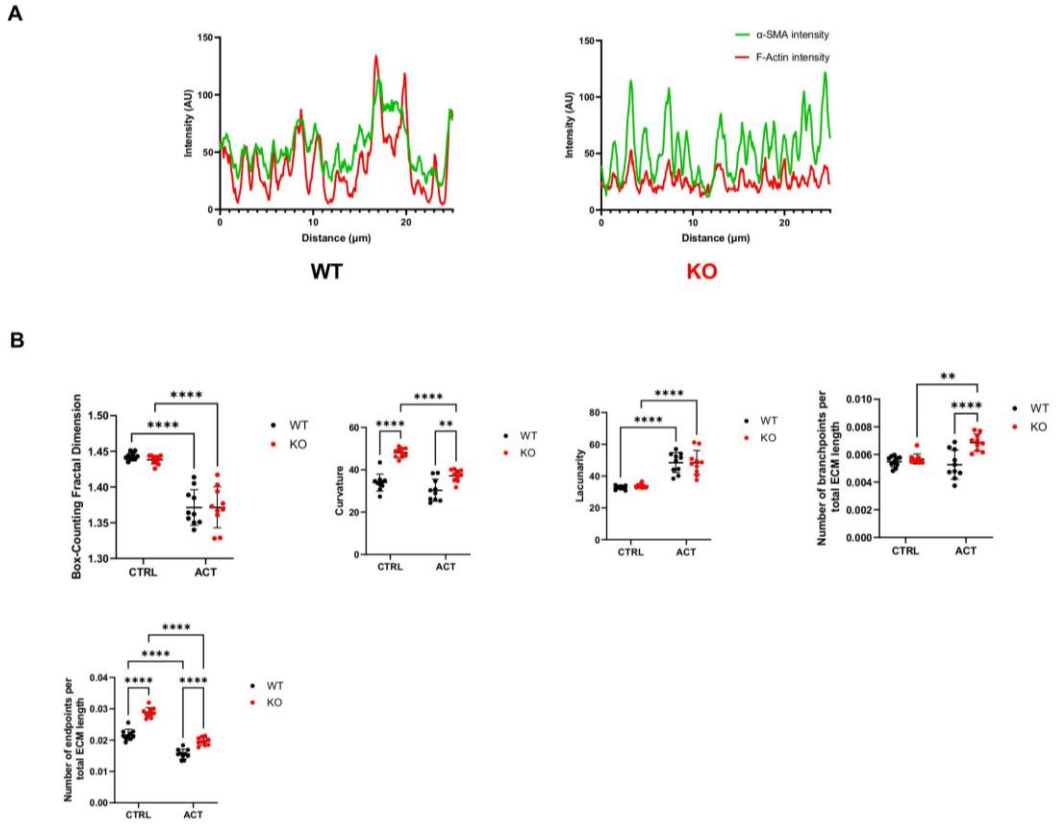

Supplementary Figure 4. Characterization of the expression of F-actin and α-SMA in stress fibers of activated YAP WT and KO CFbs and their deposited ECM. (A) Signal distribution plots of α-SMA and F-actin from stress fibers of activated YAP WT and KO CFbs. (**B)** Dotplots of Box-counting fractal dimension, lacunarity, curvature and number of branchpoints and endpoints per ECM length obtained from dECM from YAP WT and KO CFbs in control and activation conditions. Statistical analysis performed by 2-way ANOVA, followed by Tukey's multiple comparisons test.

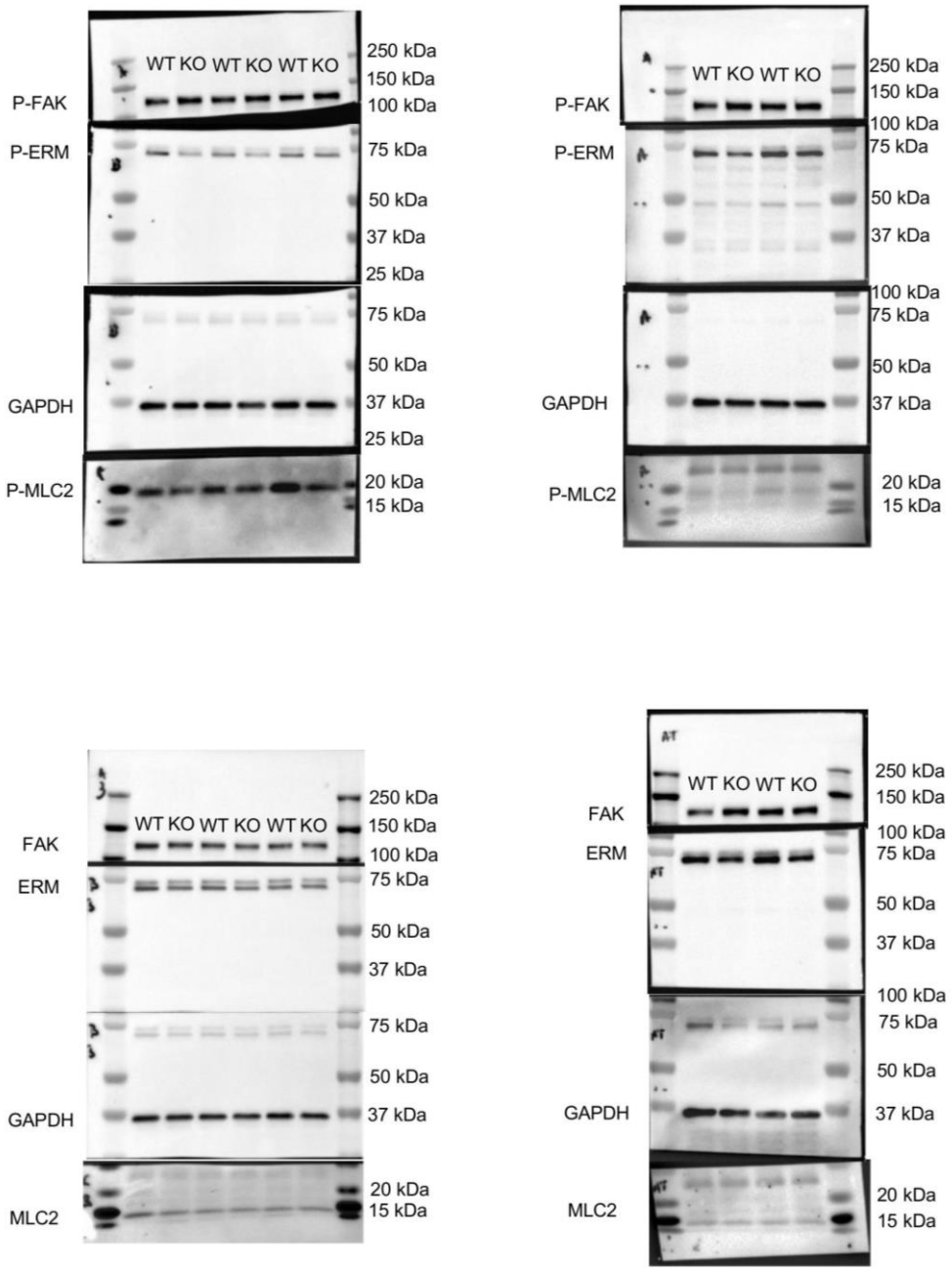

Supplementary Figure 5. Uncropped Western Blots of all quantified markers

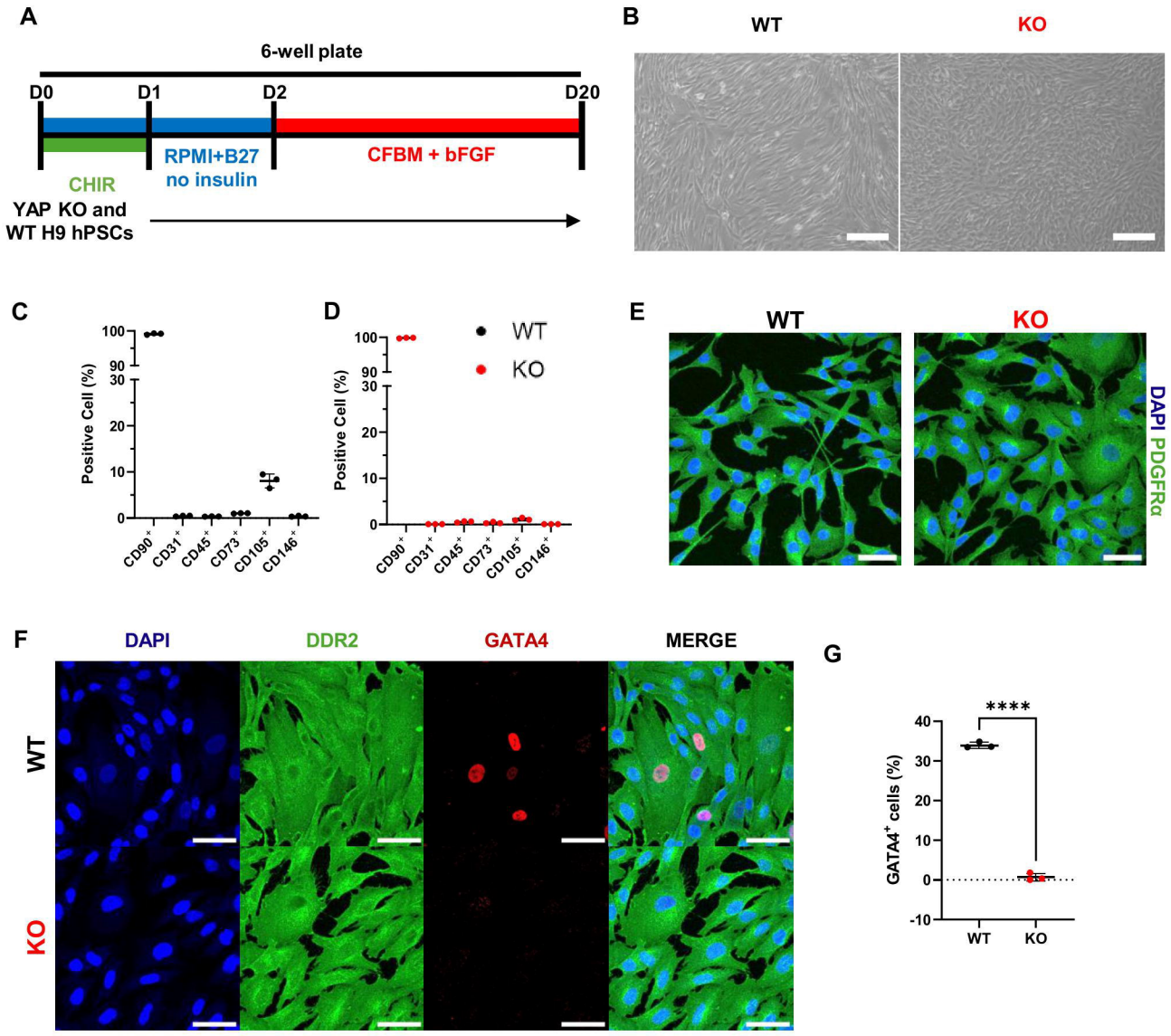
A
6-well plate
D0
D1
D2
D20
CHIR
RPMI+B27
no insulin
CFBM + bFGF
YAP KO and
WT H9 hPSCs
B
WT
KO
C
Positive Cell (%)
CD90+
CD31+
CD45+
CD73+
CD105+
CD146+
D
WT
KO
E
WT
KO
DAPI PDGFRα
F
DAPI
DDR2
GATA4
MERGE
WT
KO
G
****
GATA4+ cells (%)
WT
KO

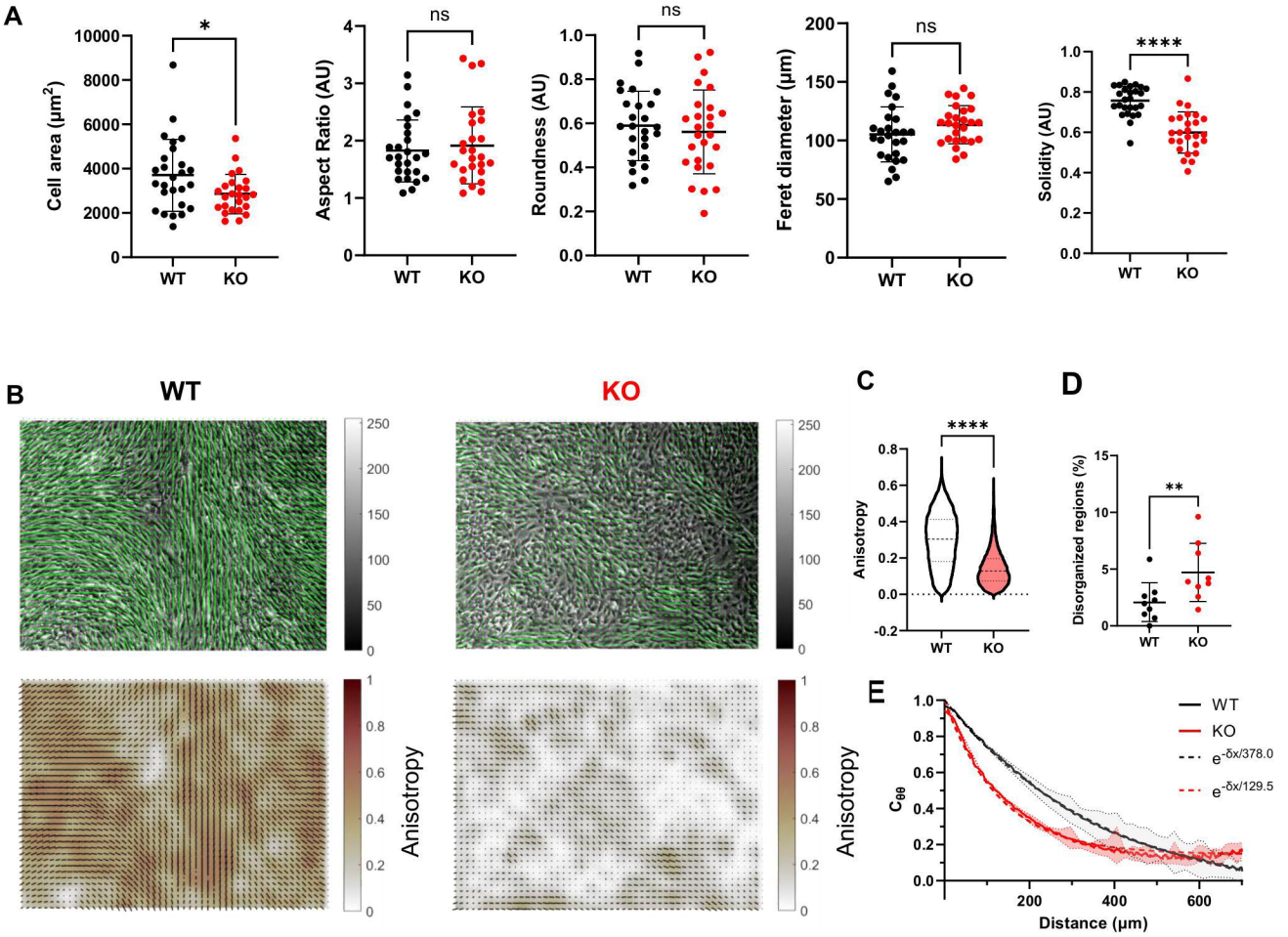
A
Cell area (μm²)
Aspect Ratio (AU)
Roundness (AU)
Feret diameter (μm)
Solidity (AU)
WT
KO
ns
*
****
B
WT
KO
Anisotropy
C
Anisotropy
D
Disorganized regions (%)
**
E
WT
KO
e^-δx/378.0
e^-δx/129.5
C_θθ
Distance (μm)

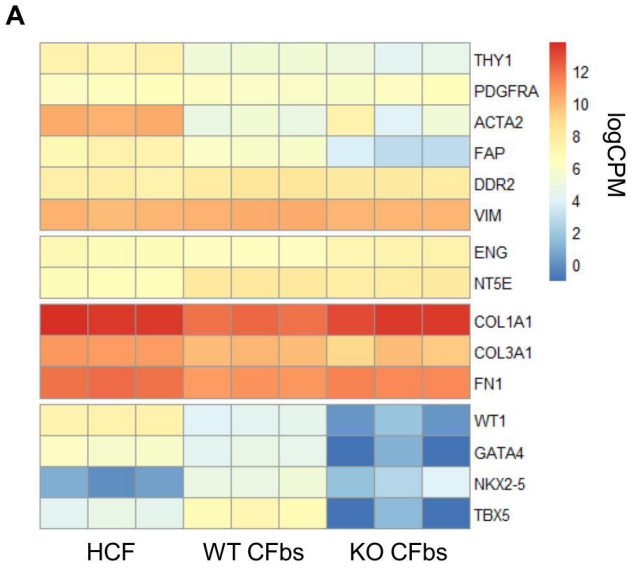
A
THY1
PDGFRA
ACTA2
FAP
DDR2
VIM
ENG
NT5E
COL1A1
COL3A1
FN1
WT1
GATA4
NKX2-5
TBX5
HCF
WT CFbs
KO CFbs
logCPM
12
10
8
6
4
2
0

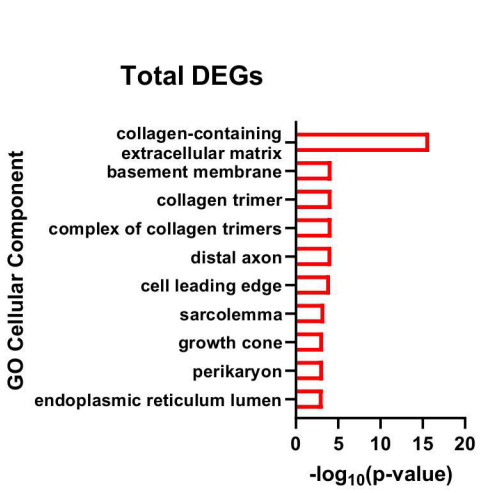
B
Total DEGs
GO Cellular Component
collagen-containing extracellular matrix
basement membrane
collagen trimer
complex of collagen trimers
distal axon
cell leading edge
sarcolemma
growth cone
perikaryon
endoplasmic reticulum lumen
0
5
10
15
20
-log10(p-value)

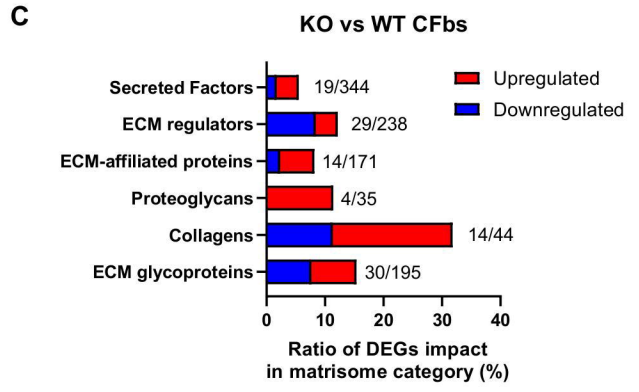
C
KO vs WT CFbs
Upregulated
Downregulated
Secreted Factors
19/344
ECM regulators
29/238
ECM-affiliated proteins
14/171
Proteoglycans
4/35
Collagens
14/44
ECM glycoproteins
30/195
0
10
20
30
40
Ratio of DEGs impact in matrisome category (%)

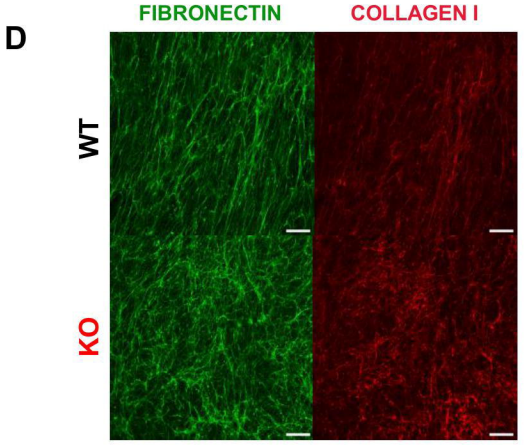
D
FIBRONECTIN
COLLAGEN I
WT
KO

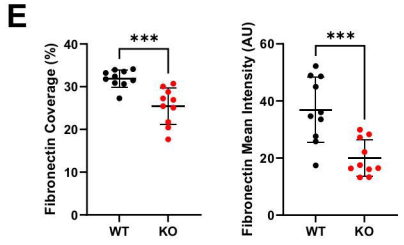
E
Fibronectin Coverage (%)
***
WT
KO
Fibronectin Mean Intensity (AU)
***
WT
KO

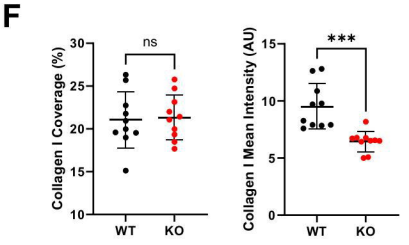
F
Collagen I Coverage (%)
ns
WT
KO
Collagen I Mean Intensity (AU)
***
WT
KO

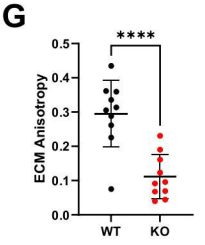
G
ECM Anisotropy
****
WT
KO

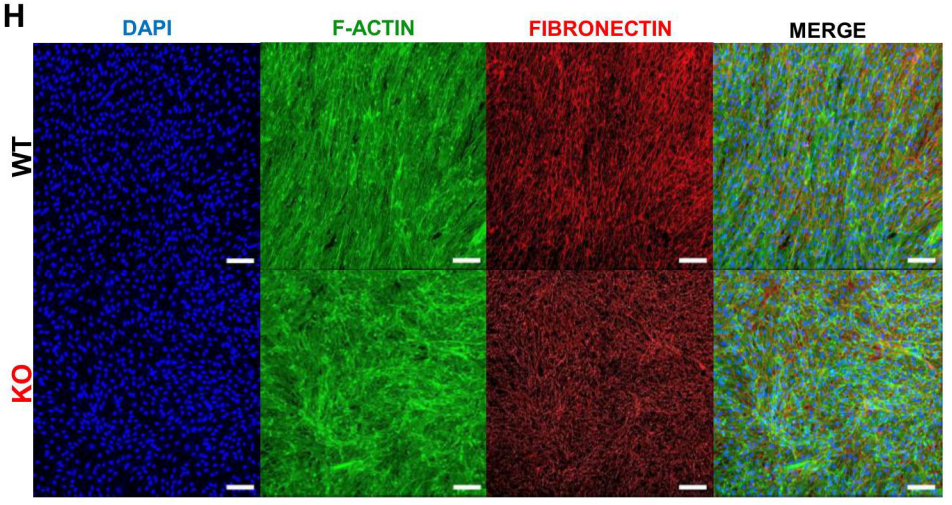
H
DAPI
F-ACTIN
FIBRONECTIN
MERGE
WT
KO

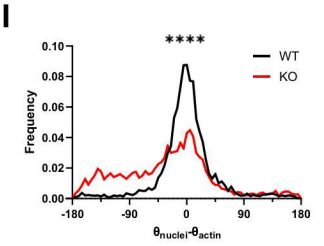
I
****
WT
KO
Frequency
θnuclei-θactin

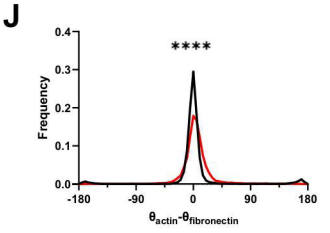
J
****
Frequency
θactin-θfibronectin

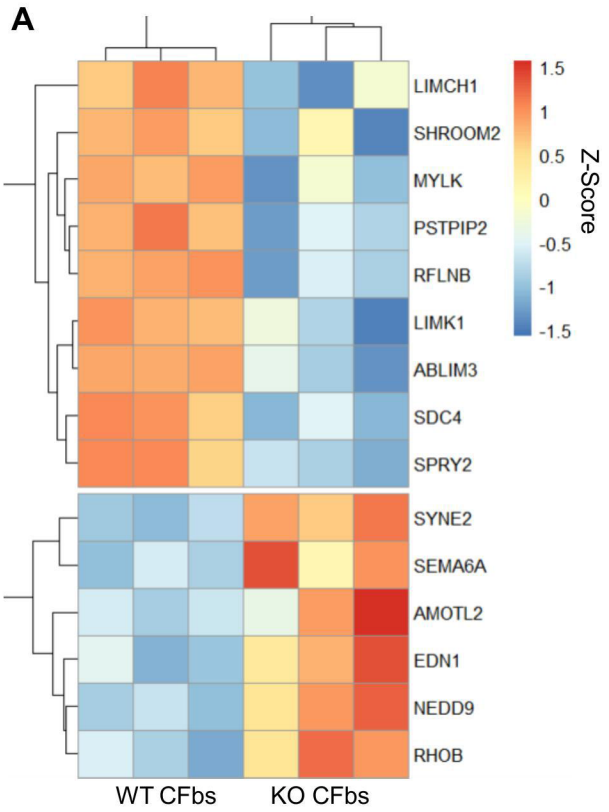
A
LIMCH1
SHROOM2
MYLK
PSTPIP2
RFLNB
LIMK1
ABLIM3
SDC4
SPRY2
SYNE2
SEMA6A
AMOTL2
EDN1
NEDD9
RHOB
WT CFbs
KO CFbs
Z-Score
1.5
1
0.5
0
-0.5
-1
-1.5

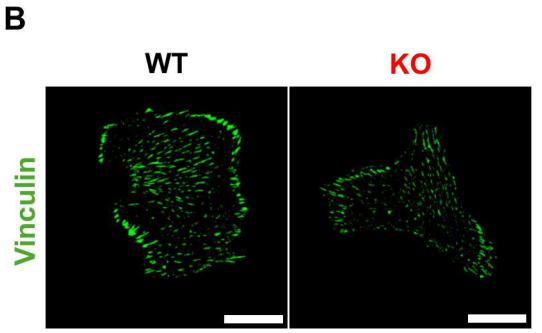
B
WT
KO
Vinculin

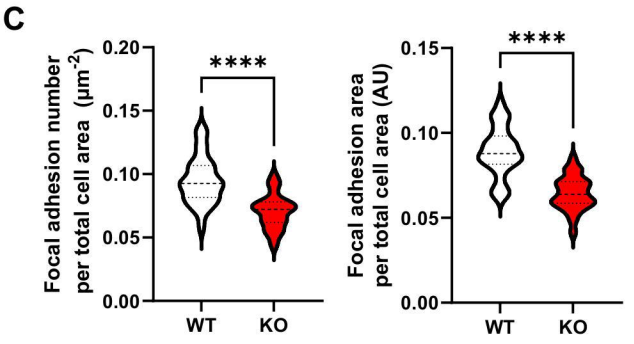
C
Focal adhesion number per total cell area (μm-2)
0.20
0.15
0.10
0.05
0.00
****
WT
KO
Focal adhesion area per total cell area (AU)
0.15
0.10
0.05
0.00
****
WT
KO

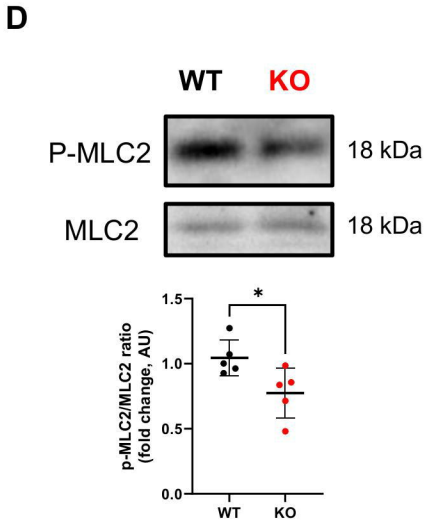
D
WT
KO
P-MLC2
18 kDa
MLC2
18 kDa
p-MLC2/MLC2 ratio (fold change, AU)
1.5
1.0
0.5
0.0
*
WT
KO

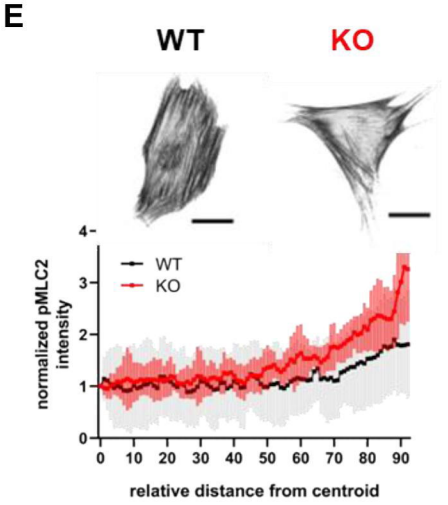
E
WT
KO
normalized pMLC2 intensity
4
3
2
1
0
WT
KO
0
10
20
30
40
50
60
70
80
90
relative distance from centroid

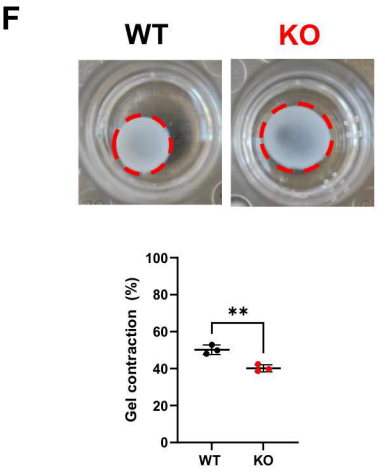
F
WT
KO
Gel contraction (%)
100
80
60
40
20
0
**
WT
KO

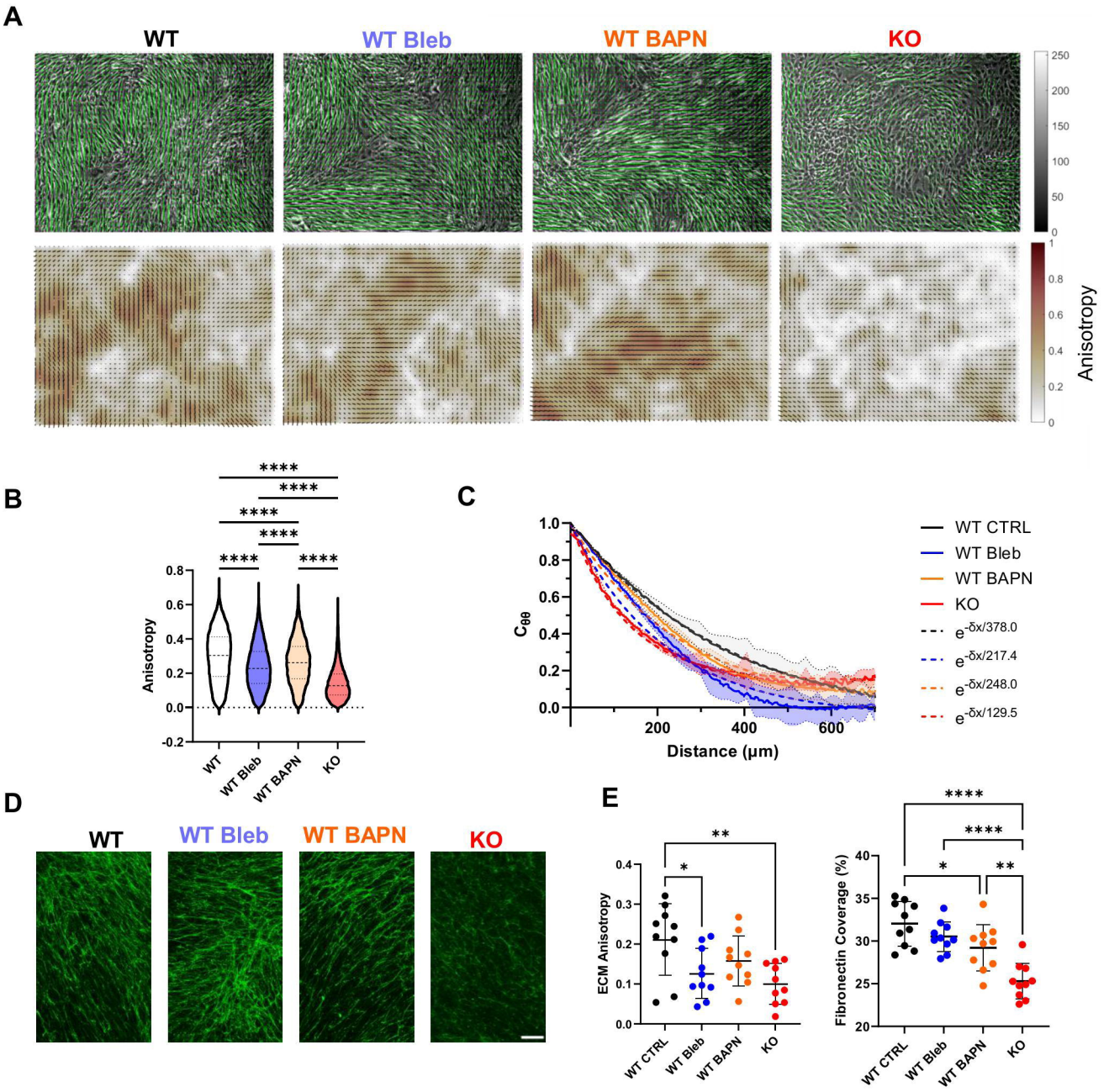
A
WT
WT Bleb
WT BAPN
KO
250
200
150
100
50
0
1
0.8
0.6
0.4
0.2
0
Anisotropy
B
****
****
****
****
****
****
Anisotropy
0.8
0.6
0.4
0.2
0.0
-0.2
WT
WT Bleb
WT BAPN
KO
C
$C_{\theta\theta}$
1.0
0.8
0.6
0.4
0.2
0.0
200
400
600
Distance (μm)
WT CTRL
WT Bleb
WT BAPN
KO
$e^{-\delta x/378.0}$
$e^{-\delta x/217.4}$
$e^{-\delta x/248.0}$
$e^{-\delta x/129.5}$
D
WT
WT Bleb
WT BAPN
KO
E
**
*
ECM Anisotropy
0.4
0.3
0.2
0.1
0.0
WT CTRL
WT Bleb
WT BAPN
KO
****
****
*
**
Fibronectin Coverage (%)
40
35
30
25
20
WT CTRL
WT Bleb
WT BAPN
KO

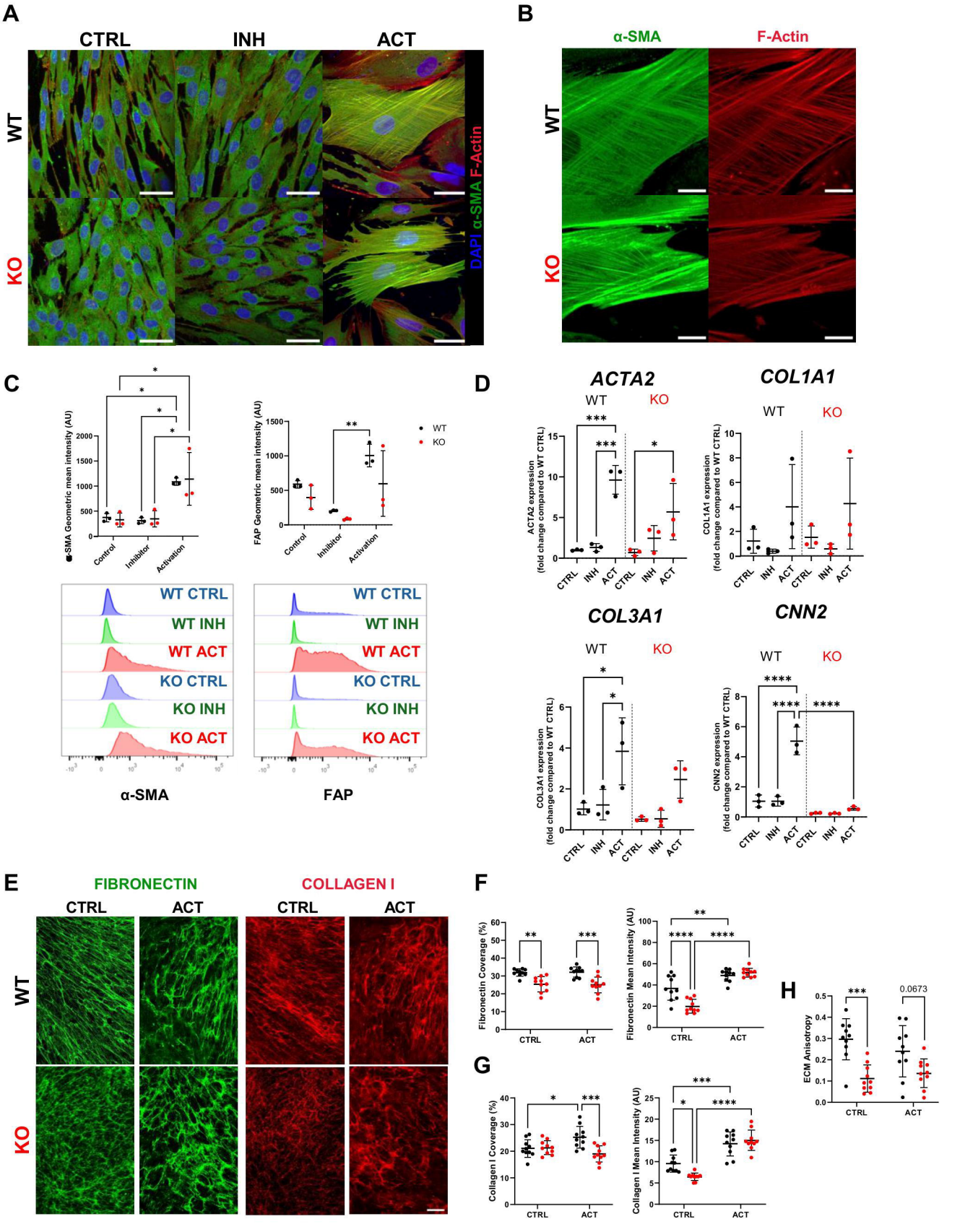
A
CTRL
INH
ACT
WT
KO
DAPI α-SMA F-Actin
B
α-SMA
F-Actin
WT
KO
C
α-SMA Geometric mean intensity (AU)
Control
Inhibitor
Activation
FAP Geometric mean intensity (AU)
WT
KO
WT CTRL
WT INH
WT ACT
KO CTRL
KO INH
KO ACT
α-SMA
FAP
D
ACTA2
COL1A1
COL3A1
CNN2
ACTA2 expression (fold change compared to WT CTRL)
COL1A1 expression (fold change compared to WT CTRL)
COL3A1 expression (fold change compared to WT CTRL)
CNN2 expression (fold change compared to WT CTRL)
CTRL
INH
ACT
E
FIBRONECTIN
COLLAGEN I
CTRL
ACT
WT
KO
F
Fibronectin Coverage (%)
Fibronectin Mean Intensity (AU)
G
Collagen I Coverage (%)
Collagen I Mean Intensity (AU)
H
ECM Anisotropy
0.0673

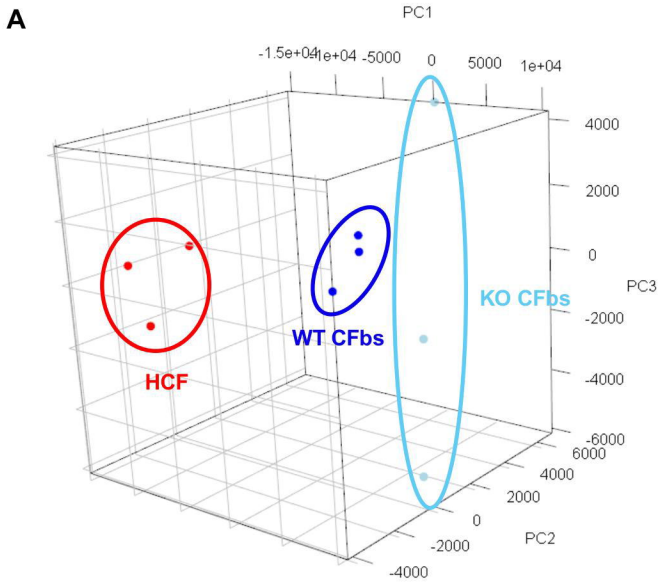
A
PC1
-1.5e+04
-1e+04
-5000
0
5000
1e+04
4000
2000
0
-2000
-4000
-6000
PC3
6000
4000
2000
0
-2000
-4000
PC2
HCF
WT CFbs
KO CFbs

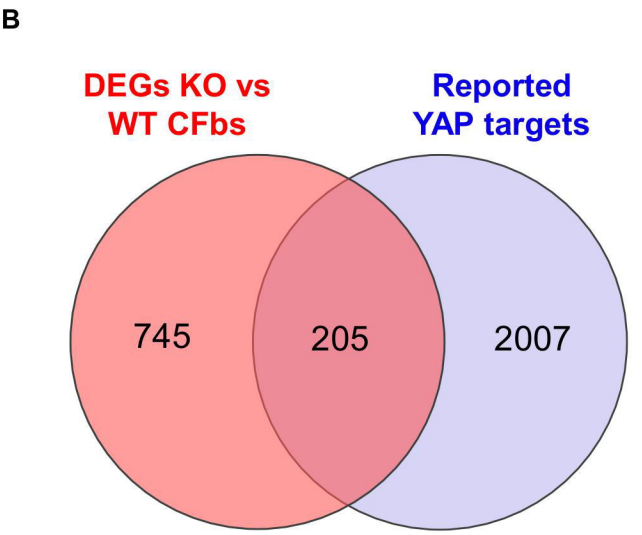
B
DEGs KO vs WT CFbs
Reported YAP targets
745
205
2007

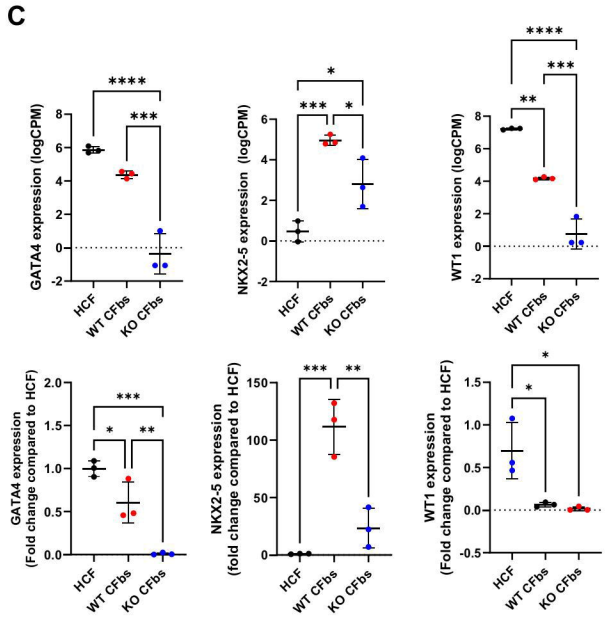
C
GATA4 expression (logCPM)
NKX2-5 expression (logCPM)
WT1 expression (logCPM)
GATA4 expression (Fold change compared to HCF)
NKX2-5 expression (fold change compared to HCF)
WT1 expression (Fold change compared to HCF)
HCF
WT CFbs
KO CFbs

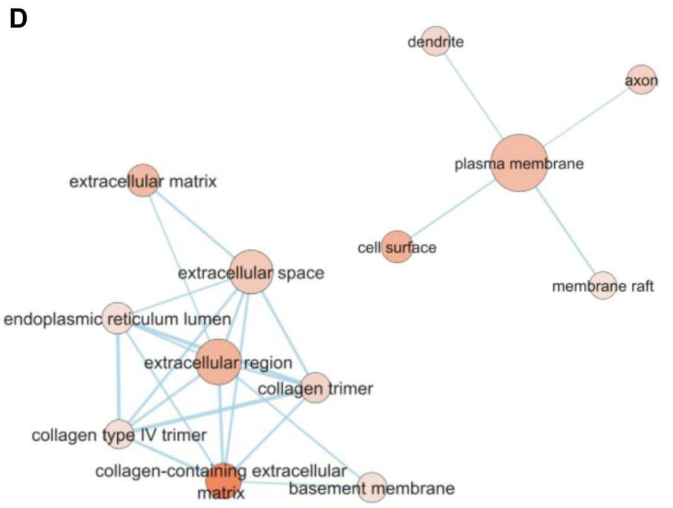
D
dendrite
axon
plasma membrane
extracellular matrix
cell surface
extracellular space
membrane raft
endoplasmic reticulum lumen
extracellular region
collagen trimer
collagen type IV trimer
collagen-containing extracellular matrix
basement membrane

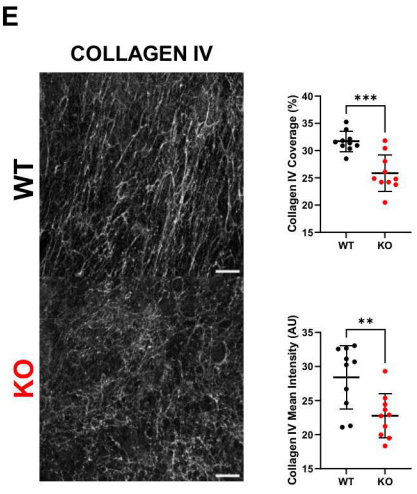
E
COLLAGEN IV
WT
KO
Collagen IV Coverage (%)
Collagen IV Mean Intensity (AU)
WT
KO

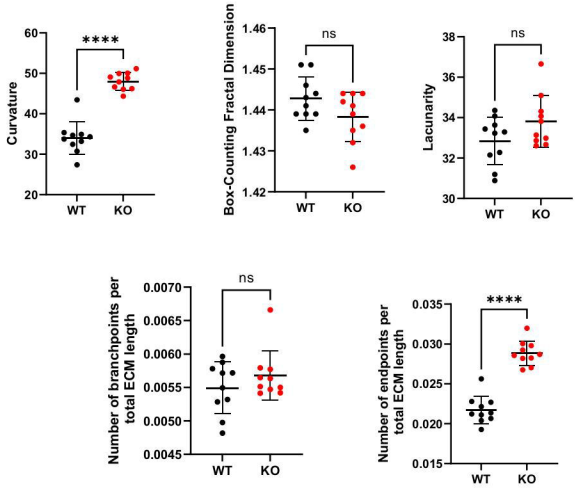
F
Curvature
Box-Counting Fractal Dimension
Lacunarity
Number of branchpoints per total ECM length
Number of endpoints per total ECM length
WT
KO
ns

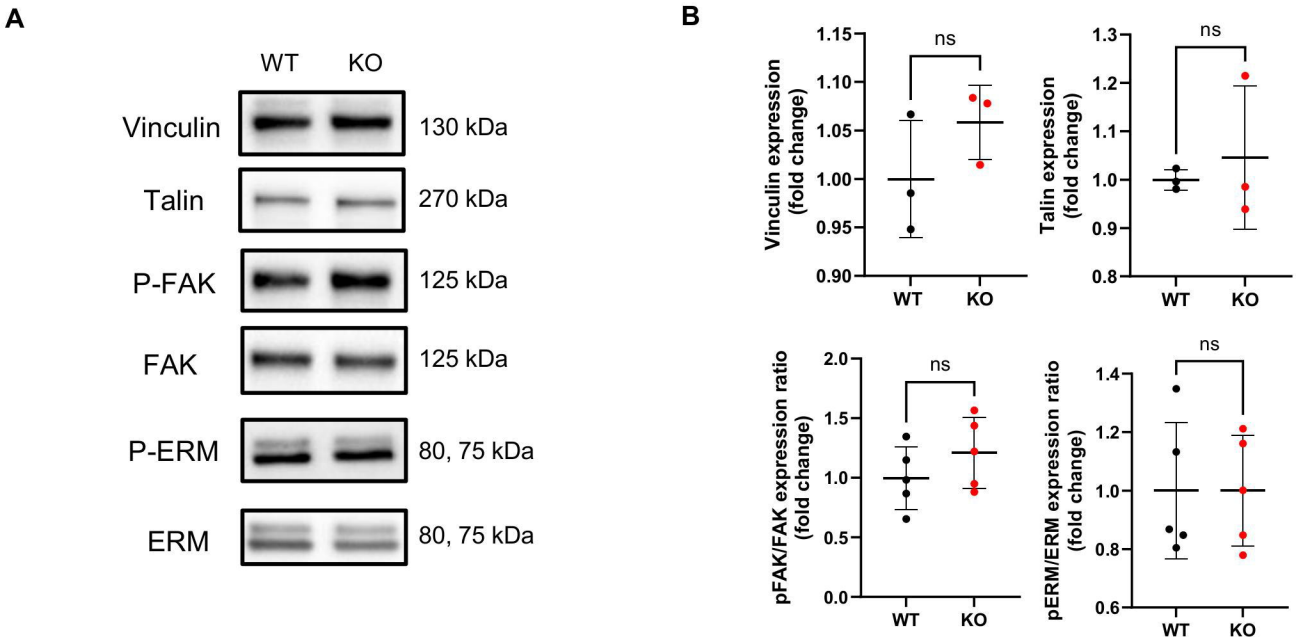
A
WT
KO
Vinculin
130 kDa
Talin
270 kDa
P-FAK
125 kDa
FAK
125 kDa
P-ERM
80, 75 kDa
ERM
80, 75 kDa
B
Vinculin expression (fold change)
ns
Talin expression (fold change)
ns
pFAK/FAK expression ratio (fold change)
ns
pERM/ERM expression ratio (fold change)
ns
WT
KO

A

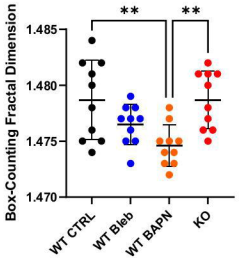
Box-Counting Fractal Dimension
1.485
1.480
1.475
1.470
**
**
WT CTRL
WT Bleb
WT BAPN
KO

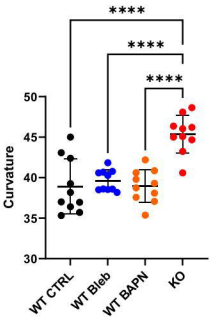
Curvature
50
45
40
35
30
****
****
****
WT CTRL
WT Bleb
WT BAPN
KO

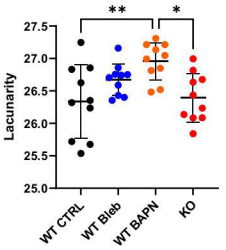
Lacunarity
27.5
27.0
26.5
26.0
25.5
25.0
**
*
WT CTRL
WT Bleb
WT BAPN
KO

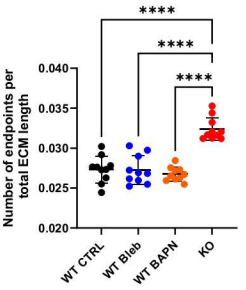
Number of endpoints per total ECM length
0.040
0.035
0.030
0.025
0.020
****
****
****
WT CTRL
WT Bleb
WT BAPN
KO

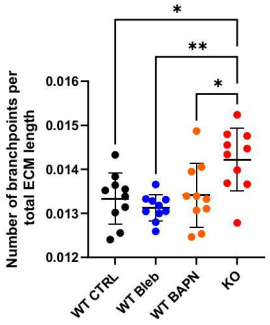
Number of branchpoints per total ECM length
0.016
0.015
0.014
0.013
0.012
*
**
*
WT CTRL
WT Bleb
WT BAPN
KO

A

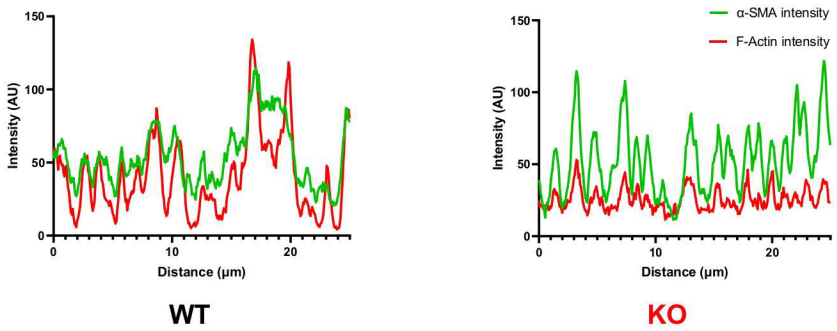
α-SMA intensity
F-Actin intensity
Intensity (AU)
Distance (μm)
WT
KO

B

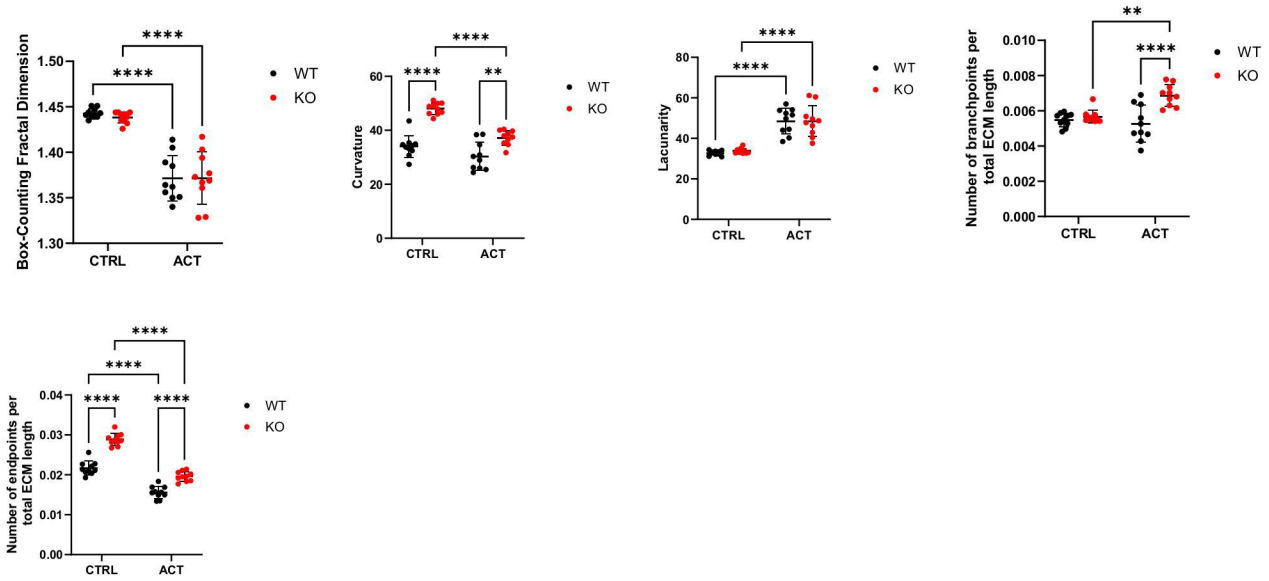
Box-Counting Fractal Dimension
Curvature
Lacunarity
Number of branchpoints per total ECM length
Number of endpoints per total ECM length
CTRL
ACT
WT
KO
****
**

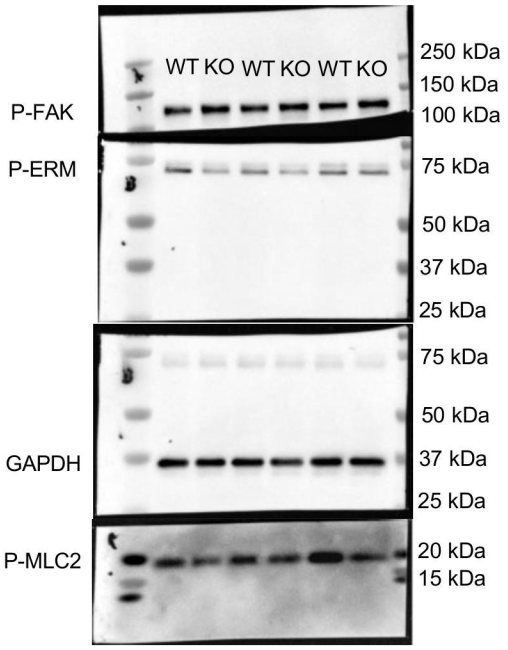
WT KO WT KO WT KO
P-FAK
P-ERM
GAPDH
P-MLC2
250 kDa
150 kDa
100 kDa
75 kDa
50 kDa
37 kDa
25 kDa
75 kDa
50 kDa
37 kDa
25 kDa
20 kDa
15 kDa

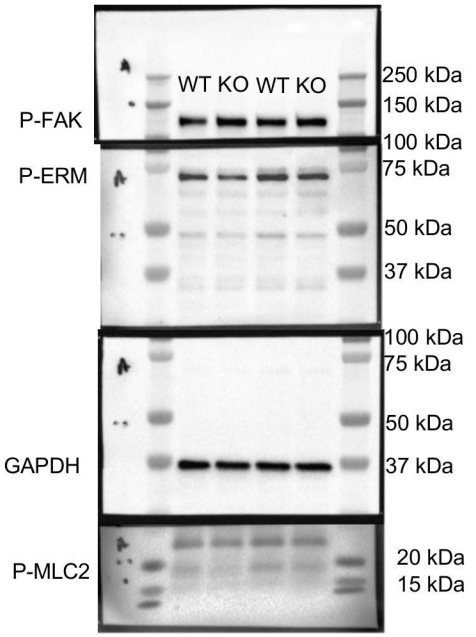
WT KO WT KO
P-FAK
P-ERM
GAPDH
P-MLC2
250 kDa
150 kDa
100 kDa
75 kDa
50 kDa
37 kDa
100 kDa
75 kDa
50 kDa
37 kDa
20 kDa
15 kDa

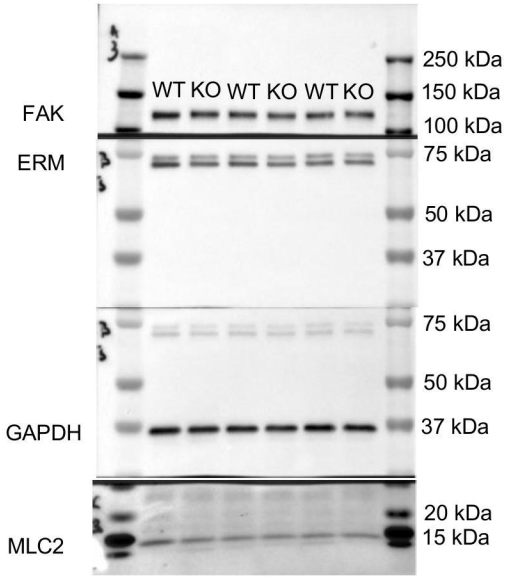
WT KO WT KO WT KO
FAK
ERM
GAPDH
MLC2
250 kDa
150 kDa
100 kDa
75 kDa
50 kDa
37 kDa
75 kDa
50 kDa
37 kDa
20 kDa
15 kDa

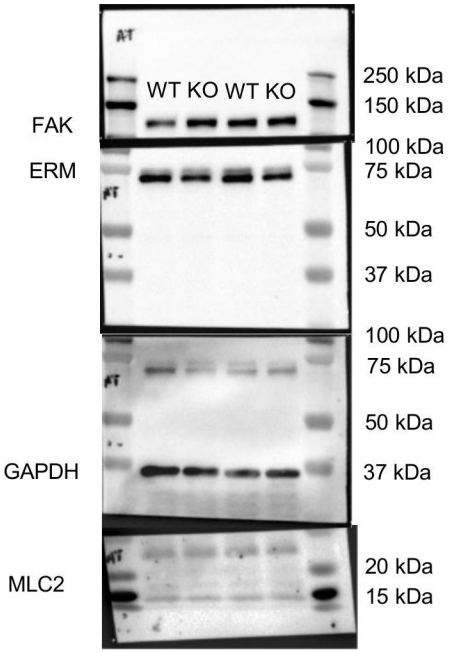
WT KO WT KO
FAK
ERM
GAPDH
MLC2
250 kDa
150 kDa
100 kDa
75 kDa
50 kDa
37 kDa
100 kDa
75 kDa
50 kDa
37 kDa
20 kDa
15 kDa